

# THE INCOMPLETE CONDITIONAL STELLAR MASS FUNCTION: UNVEILING THE STELLAR MASS FUNCTIONS OF GALAXIES AT $0.1 < z < 0.8$ FROM BOSS OBSERVATIONS

HONG GUO<sup>1</sup>, XIAOHU YANG<sup>2,3</sup>, YI LU<sup>1</sup>

*Draft version May 9, 2018*

## Abstract

We propose a novel method to constrain the missing fraction of galaxies using galaxy clustering measurements in the galaxy conditional stellar mass function (CSMF) framework, which is applicable to surveys that suffer significantly from sample selection effects. The clustering measurements, which are not sensitive to the random sampling (missing fraction) of galaxies, are widely used to constrain the stellar-halo mass relation (SHMR). By incorporating a missing fraction (incompleteness) component into the CSMF model (ICSMF), we use the incomplete stellar mass function and galaxy clustering to simultaneously constrain the missing fractions and the SHMRs. Tests based on mock galaxy catalogs with a few typical missing fraction models show that this method can accurately recover the missing fraction and the galaxy SHMR, and hence provides us reliable measurements of the galaxy stellar mass functions. We then apply it to the Baryon Oscillation Spectroscopic Survey (BOSS) over the redshift range of  $0.1 < z < 0.8$  for galaxies of  $M_* > 10^{11} M_\odot$ . We find the sample completeness for BOSS is over 80% at  $z < 0.6$ , but decreases at higher redshifts to about 30%. After taking these completeness factors into account, we provide accurate measurements of the stellar mass functions for galaxies with  $10^{11} M_\odot < M_* < 10^{12} M_\odot$ , as well as the SHMRs, over the redshift range  $0.1 < z < 0.8$  in this largest galaxy redshift survey.

*Subject headings:* cosmology: observations — cosmology: theory — galaxies: distances and redshifts — galaxies: halos — galaxies: statistics — large-scale structure of universe

## 1. INTRODUCTION

The connection between the galaxy properties and those of the dark matter has been investigated in depth in the past decades for the local and high-redshift galaxies (see e.g., Norberg et al. 2001; Zehavi et al. 2002; Zehavi et al. 2005, 2011; Yang et al. 2003; Yang et al. 2004, 2007; Zheng et al. 2007; Moster et al. 2010, 2013; Coupon et al. 2012; Leauthaud et al. 2012; Guo et al. 2014; McCracken et al. 2015). The galaxy stellar-halo mass relation (SHMR), in particular, provides important constraints to the galaxy formation and evolution models (see e.g., Yang et al. 2009, 2012; Moster et al. 2010, 2013; Behroozi et al. 2013a; Beutler et al. 2013; Reddick et al. 2013; Lin et al. 2016; Zu & Mandelbaum 2015, 2016; Wang et al. 2018), as it probes the joint-evolution of the galaxy and halo mass growth histories and is directly related to the cosmic star formation histories (see e.g., Behroozi et al. 2013a; Yang et al. 2013).

There are multiple ways of determining the halo masses for galaxies of different stellar masses. The common methods include the halo occupation distribution (HOD) (see e.g., Jing et al. 1998; Peacock & Smith 2000; Seljak 2000; Scoccimarro et al. 2001; Berlind & Weinberg 2002; Berlind et al. 2003; Zehavi et al. 2005; Zheng et al. 2005; Zheng et al. 2007; Zheng et al. 2009; Guo et al. 2014; Guo et al. 2015; McCracken et al. 2015) and conditional

stellar mass function (CSMF) (see e.g., Yang et al. 2009, 2012; More 2012; Cacciato et al. 2013; More et al. 2013; Reddick et al. 2013; van den Bosch et al. 2008, 2013; Yang et al. 2017) modeling of the galaxy clustering measurements, the subhalo abundance matching models (see e.g., Rodríguez-Puebla et al. 2012, 2017; Behroozi et al. 2013a; Moster et al. 2013; Guo et al. 2016), and the direct weak gravitational lensing measurements (see e.g., Mandelbaum et al. 2006; Miyatake et al. 2015; Zu & Mandelbaum 2015). The central galaxy SHMR has been extensively studied with these methods for galaxy samples at different redshifts, and is found to follow a broken power law relation with a steep slope for low mass halos of  $M < 10^{12} M_\odot$  and becoming much flatter for more massive halos (Yang et al. 2009, 2012; Moster et al. 2010, 2013; Wang & Jing 2010). Within all these probes, a crucial measurement is the galaxy stellar mass function (SMF).

Thanks to the large-scale galaxy redshift surveys, e.g., the 2dF Galaxy Redshift Survey (2dFGRS; Colless 1999) and the Sloan Digital Sky Survey (SDSS; York et al. 2000), at the low redshifts of  $z < 0.2$ , we are able to accurately measure the galaxy stellar mass function (see e.g., Bell et al. 2003; Li & White 2009; Bernardi et al. 2010, 2013) and the SHMR (see e.g., Yang et al. 2009, 2012; Wang et al. 2007; Moster et al. 2010, 2013; Behroozi et al. 2013a; Rodríguez-Puebla et al. 2017). At higher redshifts, the measurements of the galaxy SMFs in literature have much larger uncertainties compared to the low-redshift ones, because the galaxy SMFs at high redshifts are mostly derived from deep photometric surveys covering small sky area, where the sample variance effect would dominate the error budget (Davidzon et al. 2013, 2017; Ilbert et al. 2013; Maraston et al. 2013;

<sup>1</sup> Key Laboratory for Research in Galaxies and Cosmology, Shanghai Astronomical Observatory, Shanghai 200030, China; guohong@shao.ac.cn

<sup>2</sup> Department of Astronomy, Shanghai Key Laboratory for Particle Physics and Cosmology, Shanghai Jiao Tong University, Shanghai 200240, China

<sup>3</sup> IFSA Collaborative Innovation Center, and Tsung-Dao Lee Institute, Shanghai Jiao Tong University, Shanghai 200240, China

Muzzin et al. 2013; Moustakas et al. 2013; Tomczak et al. 2014; Santini et al. 2015). For example, as summarized in Table 1 of Rodríguez-Puebla et al. (2017) (see also Table 3 of Behroozi et al. 2013a), the galaxy SMF at  $0.2 < z < 1$  is measured with the largest volume in Moustakas et al. (2013) using the PRISM MUlti-object Survey (PRIMUS; Coil et al. 2011) covering an area of  $9 \text{ deg}^2$ .

As constraints to the galaxy SHMR are generally obtained from fitting the galaxy SMFs with or without the spatial clustering measurements, models of the SHMR for higher-redshift galaxies thus have significant differences among different studies, although they agree with each other within errors for low-redshift galaxies (see e.g., Shankar et al. 2014). The difference is more significant for massive galaxies of  $M_* > 10^{11} M_\odot$ . For example, the SHMR model of Yang et al. (2012) would predict a high-mass end slope of  $M_* \propto M^{0.375}$  for galaxies at  $z = 0.5$ , while of the model of Behroozi et al. (2013a) would have  $M_* \propto M^{0.265}$ . However, the total number densities of galaxies with  $M_* > 10^{11} M_\odot$  for these two models only differ by about 20%, as the halo mass function is decreasing very fast toward the high mass end. Therefore, discriminating the different SHMR models would require accurate measurements of the galaxy SMF at the massive end, which can only be achieved with wide-area galaxy surveys. Moreover, accurate clustering measurements to constrain the SHMR models would also require a large sample volume.

Currently, the largest galaxy redshift survey at  $0.2 < z < 0.8$  is the SDSS-III Baryon Oscillation Spectroscopic Survey (BOSS; Dawson et al. 2013). The latest data release 12 of the BOSS galaxy sample covers an area of  $10,252 \text{ deg}^2$  (Reid et al. 2016), which is about 1100 times larger than that of the PRIMUS. Therefore, the dominating errors on the BOSS galaxy SMF measurements come from the systematic errors on the galaxy stellar mass measurements, rather than the sample variance effect, which only has a minor contribution. The BOSS galaxy sample would potentially provide the most accurate galaxy SMF and SHMR measurements at these intermediate redshifts. However, the main science drive for BOSS is to measure the baryonic acoustic oscillation (BAO) signals in order to constrain the cosmological parameters (see e.g., Alam et al. 2017), so the galaxy targeting strategy is to select intermediate-redshift luminous galaxies that cover a large enough volume. Due to the complicated selection criteria of both the apparent magnitude and color, the resulting galaxy sample is, however, neither volume-limited nor stellar mass complete. Thus, the measured galaxy SMFs in BOSS cannot be directly compared with those from other studies of volume-limited samples. Furthermore, the BOSS galaxy sample is also not a homogeneous sample of luminous red galaxies at the intermediate redshifts, but also purposely includes a significant fraction of blue galaxies (Maraston et al. 2013).

Efforts have been made to estimate the stellar mass completeness for the BOSS galaxies, using either galaxies selected with wider color cuts (Tinker et al. 2017) or deeper imaging observations of those massive galaxies in the Stripe 82 region (Leauthaud et al. 2016; Saito et al. 2016), with the conclusions that the high red-

shift BOSS galaxies are significantly affected by the mass incompleteness. In fact, the mass incompleteness caused by the complicated target selection is not just the concern of BOSS. It has become a common issue for many large-scale galaxy redshift surveys targeting at high-redshift objects. For example, the on-going SDSS-IV extended Baryon Oscillation Spectroscopic Survey (eBOSS; Dawson et al. 2016), targeting at the luminous red galaxies (LRG; Prakash et al. 2016) and emission line galaxies (ELG; Raichoor et al. 2017) in the redshift range of  $0.7 < z < 1.1$  adopts various apparent magnitude and color cuts to select objects for further spectroscopic observations. Similar issues also happen for many of the next-generation galaxy redshift surveys, such as the Dark Energy Spectroscopic Instrument (DESI; DESI Collaboration et al. 2016) and Prime Focus Spectrograph (PFS; Takada et al. 2014).

Naturally, it is more reliable to constrain the missing fraction of galaxies caused by the complicated target selections without resort to external measurements from other surveys. Montero-Dorta et al. (2016) presented a forward-modeling technique to quantify the completeness of BOSS galaxies in the red sequence at  $z \sim 0.55$ . By matching the observed color-magnitude distributions with reasonable analytical parametric models convolved with the photometric errors and selection effects, it is possible to derive the intrinsic color-magnitude distribution and therefore estimate the completeness as a function of magnitude. In this paper, we propose a novel method to constrain the completeness by making use of a clustering measurement property—the galaxy clustering is insensitive to the random sampling (missing fraction) of galaxies. On the other hand, within the CSMF framework, accurate clustering measurements can be used to constrain the SHMR. We can therefore incorporate a missing fraction component in the SHMR, so that both the SHMR and the missing fraction of galaxies can be simultaneously constrained. We used mock galaxy catalogs with a few typical missing fraction models to demonstrate the reliability of such a method and then apply it to the BOSS galaxy sample to provide so far the most accurate measurements of the galaxy SMFs and SHMRs at massive end in the redshift range of  $0.1 < z < 0.8$ .

The structure of the paper is constructed as follows. In §2, we describe the galaxy samples and the simulation used in the modeling. We introduce our modeling method in §3 and test it in §4. We present the modeling results for the BOSS galaxies in §5 and discuss our models in §6. We summarize our results in §7. Throughout this paper, we assume a spatially flat  $\Lambda$  cold dark matter cosmology, with  $\Omega_m = 0.307$ ,  $h = 0.678$ ,  $\Omega_b = 0.048$  and  $\sigma_8 = 0.823$ , consistent with the constraints from Planck (Planck Collaboration 2014) and with the parameters used in the simulation adopted for our modeling (see §2). For the stellar mass estimates, we assume a universal Chabrier (2003) initial mass function (IMF), the stellar population synthesis model of Bruzual & Charlot (2003) and the time-dependent dust attenuation model of Charlot & Fall (2000). All masses are in units of  $M_\odot$ .

## 2. DATA

### 2.1. BOSS Galaxy Sample

We use the Data Release 12 of the BOSS galaxy sample, with redshifts for 1,372,737 galaxies over an area of  $10,252 \text{ deg}^2$  (Reid et al. 2016). The detailed descriptions of the survey can be found in Eisenstein et al. (2011) and Dawson et al. (2013). The BOSS galaxy sample is formally divided into two subsamples with different target selections focusing on galaxies at low and high redshifts. The target selections are based on following set of combinations of model magnitudes,

$$c_{\parallel} = 0.7(g - r) + 1.2(r - i - 0.18), \quad (1)$$

$$c_{\perp} = (r - i) - (g - r)/4 - 0.18, \quad (2)$$

$$d_{\perp} = (r - i) - (g - r)/8, \quad (3)$$

where the  $g - r$  and  $r - i$  colors are based on the `model` magnitudes.

The low redshift sample, denoted as LOWZ, is an extension to the SDSS-II LRG sample (Eisenstein et al. 2001) to fainter magnitudes in  $0.15 < z < 0.43$ , with the selection cuts of

$$|c_{\perp}| < 0.2, \quad (4)$$

$$r < 13.6 + c_{\parallel}/0.3, \quad (5)$$

$$16 < r < 19.6, \quad (6)$$

where  $r$  is based on the `model` magnitude. As clearly shown in Figure 11 of Eisenstein et al. (2001), most of the galaxies selected with the above cuts in LOWZ would be LRGs.

The higher redshift sample, denoted as CMASS, targets galaxies that roughly follow a constant stellar mass cut in the redshift range of  $0.43 < z < 0.7$  (Maraston et al. 2013). The corresponding selection cuts are

$$|d_{\perp}| > 0.55, \quad (7)$$

$$i < 19.86 + 1.6(d_{\perp} - 0.8), \quad (8)$$

$$17.5 < i < 19.9, \quad (9)$$

where the magnitude  $i$  is the  $i$ -band `model` magnitude.

To increase the stellar mass completeness at different redshifts, we use the combined sample of LOWZ and CMASS. The redshift and angular distribution of the combined BOSS galaxy sample are presented in Reid et al. (2016) (their Figures 8 and 11). The sky coverage of the LOWZ sample in the northern galactic cap (NGC) is slightly smaller than that of CMASS, due to the removal of data observed in the first nine months that have the incorrect star-galaxy separation cut applied. At  $z < 0.4$ , as there is only a small fraction of CMASS galaxies in this redshift range, we include all LOWZ galaxies and those CMASS galaxies that fall into the LOWZ geometry mask (covering about  $9000 \text{ deg}^2$ ). At  $z > 0.4$ , the different angular distributions of LOWZ and CMASS are taken into account by combining the random catalogs for the two samples when measuring the spatial clustering.

As we have a combined sample covering a large redshift range of  $0.1 < z < 0.8$ , we divide the galaxies into different redshift intervals with a bin size of  $\Delta z = 0.1$  to study the evolution of these massive galaxies. In total, we have seven redshift bins, with the detailed information displayed in Table 1, where the total number of galaxies,  $N_{\text{tot}}$ , the average sample stellar mass with the corresponding scatter,  $\langle \log M_* \rangle$ , and the mean number density,  $\bar{n}_g$ , are shown for each sample. As the

TABLE 1  
SAMPLES OF DIFFERENT REDSHIFT BINS

redshift range	$N_{\text{tot}}$	$\langle \log(M_*/M_{\odot}) \rangle$	$\bar{n}_g/(h^3 \text{ Mpc}^{-3})$
$0.1 < z < 0.2$	84404	$11.02 \pm 0.12$	$5.71 \times 10^{-4}$
$0.2 < z < 0.3$	117822	$11.10 \pm 0.12$	$3.25 \times 10^{-4}$
$0.3 < z < 0.4$	179726	$11.30 \pm 0.12$	$2.84 \times 10^{-4}$
$0.4 < z < 0.5$	294291	$11.31 \pm 0.14$	$2.80 \times 10^{-4}$
$0.5 < z < 0.6$	398565	$11.28 \pm 0.15$	$2.85 \times 10^{-4}$
$0.6 < z < 0.7$	172251	$11.37 \pm 0.16$	$0.99 \times 10^{-4}$
$0.7 < z < 0.8$	30954	$11.64 \pm 0.69$	$0.15 \times 10^{-4}$

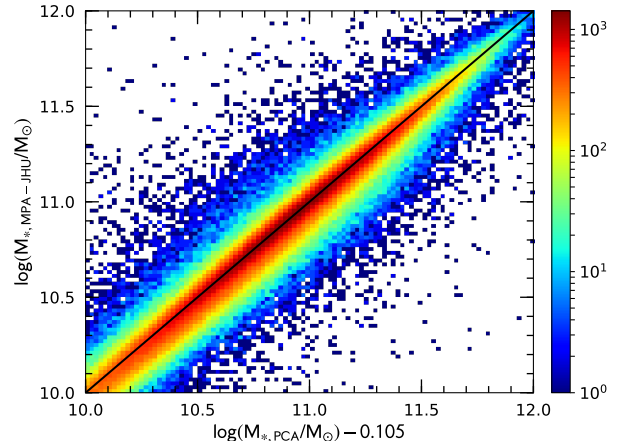


FIG. 1.— Comparisons between the stellar masses derived from the PCA method of Chen et al. (2012) and those from the MPA-JHU catalog. The PCA stellar masses are systematically overestimated by 0.105 dex. The color scale shows the density distribution.

galaxy SMF and SHMR have been studied extensively in  $0.1 < z < 0.2$  with the SDSS DR7 Main galaxy sample, in this paper we focus on the measurements in  $0.2 < z < 0.8$ , and use the low-redshift measurements as a consistency check with the literature.

The galaxy stellar mass used in this paper is estimated in Chen et al. (2012) by fitting the galaxy spectra over the rest-frame wavelength range of  $3700\text{--}5500\text{\AA}$  with the principal component analysis (PCA) method. We use the stellar mass obtained by applying the stellar population synthesis (SPS) models of Maraston & Strömbäck (2011) with an IMF of Kroupa (2001) and a dust attenuation model of Charlot & Fall (2000). The total galaxy stellar mass is obtained by applying the mass-to-light ratio within the fiber aperture to the whole galaxy. We refer the readers to Chen et al. (2012) for details.

At low redshifts, the BOSS sample (especially LOWZ) has a significant overlap with the SDSS DR7 Main galaxy sample (Abazajian et al. 2009), where the galaxy stellar masses have been derived in the MPA-JHU catalog<sup>4</sup> following the method of Kauffmann et al. (2003) by applying the SPS model of Bruzual & Charlot (2003). In order to compare with the literature for low-redshift measurements of the galaxy SHMR and SMFs, we cross-match the two galaxy samples and show the comparisons of the stellar masses in the different catalogs in Figure 1. The stellar masses with the PCA method are systematically overestimated by 0.105 dex compared to the MPA-JHU stellar masses, due to the truncated star formation histories and a smaller fraction of galaxies with recent bursts

<sup>4</sup> <https://wwwmpa.mpa-garching.mpg.de/SDSS/DR7/>

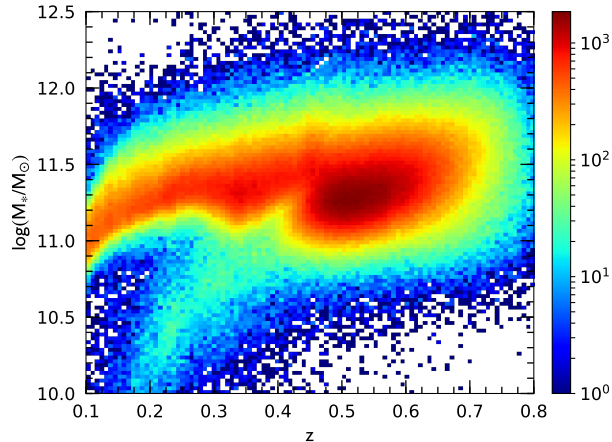


FIG. 2.— Stellar mass distribution as a function of redshift  $z$  for the combined LOWZ+CMASS sample. The color scale shows the density distribution.

(see Figures 12 and 13 of [Chen et al. 2012](#), and discussions therein). We also apply the standard correction of a constant shift of  $-0.05$  dex ([Bernardi et al. 2010](#)) to convert from a [Kroupa \(2001\)](#) IMF to that of [Chabrier \(2003\)](#). Therefore, in this paper we reduce the galaxy stellar masses in [Chen et al. \(2012\)](#) by  $0.155$  dex to be consistent with literature.

We show in Figure 2 the stellar mass distribution as a function of redshift for the combined sample. The majority of the BOSS galaxies are more massive than  $10^{11} M_{\odot}$ . We can therefore accurately measure the massive end of the galaxy SMF and model the corresponding SHMR. As the redshift increases, the average galaxy stellar mass moves toward slightly more massive end due to the flux limit of the sample selection criteria. In order to study the evolution of galaxy SMF in a broad redshift range, we only focus on the massive galaxies with  $M_* > 10^{11} M_{\odot}$  in this paper.

As will be demonstrated in the following sections, although red and blue galaxies could have different selection functions, the derived total galaxy SMFs and the SHMRs using the whole BOSS sample are not affected, even if we only select homogeneous red galaxy samples in our measurements. Because the red galaxies dominate the contribution to the SMF for  $M_* > 10^{11} M_{\odot}$  (see e.g., Figure 10 of [Moustakas et al. 2013](#)), the small fraction of blue galaxies in BOSS would not have any significant effect on the SHMR for the whole galaxy sample, even though red and blue galaxies tend to have slightly different SHMRs.

## 2.2. Dark Matter Simulation

In order to evaluate our method in constraining the missing fraction of galaxies, we use the dark matter halos extracted from the BigMultidark Planck simulation (BigMDPL<sup>5</sup>; [Klypin et al. 2016](#)), with the cosmological parameters of  $\Omega_m = 0.307$ ,  $\Omega_b = 0.048$ ,  $h = 0.678$ ,  $n_s = 0.96$  and  $\sigma_8 = 0.823$ . The simulation has a box size of  $2.5 h^{-1} \text{Gpc}$  and a mass resolution of  $2.4 \times 10^{10} h^{-1} M_{\odot}$ . It has been used to construct mock galaxy catalogs for the CMASS sample ([Rodríguez-Torres et al. 2016](#)). The dark matter halos and subhalos in the simulation are

identified with the ROCKSTAR phase-space halo finder ([Behroozi et al. 2013b](#)).

We use seven different redshift outputs of  $z = 0.152, 0.246, 0.347, 0.453, 0.547, 0.655,$  and  $0.759$  from BigMDPL, roughly corresponding to the median redshifts of the seven BOSS galaxy samples in the different redshift bins. The galaxy clustering and stellar mass function measurements from the different redshift bins are modeled separately using the corresponding halo catalogs in order to constrain their evolution.

## 3. METHOD

In this paper, we incorporate a incompleteness component into the CSMF (hereafter, ICSMF) framework ([Yang et al. 2012](#)) to predict the accurate galaxy total SMF and SHMR from incomplete galaxy samples as those in BOSS.

### 3.1. Theoretical Models

In this subsection, we provide the details of our ICSMF model, as well as the model predictions of the stellar mass functions and clustering properties of galaxies (i.e., the projected two pointed correlation functions).

#### 3.1.1. Incomplete Conditional Stellar Mass Function

Following [Yang et al. \(2012\)](#), we assume that the CSMF of central galaxies, i.e., the average number of central galaxies with stellar mass  $M_*$  hosted by halos of mass  $M$ , can be characterized by a log-normal distribution function, ([Yang et al. 2009](#)),

$$\Phi_c(M_*|M) = \frac{1}{\sqrt{2\pi}\sigma_c} \exp\left[-\frac{(\log M_* - \log \langle M_*|M \rangle)^2}{2\sigma_c^2}\right] \quad (10)$$

where  $\sigma_c$  is the scatter of stellar mass distribution in a given halo with mass  $M$ . The scatter is not well constrained by the SMF only (see e.g., [Moster et al. 2010](#)). It is generally assumed to be a constant value of around  $0.173$  (it is assumed to be  $0.15$  in [Moster et al. 2013](#)) for low redshifts of  $z < 0.9$  ([Yang et al. 2012](#)). Recent measurements of [Tinker et al. \(2017\)](#) suggest that the scatter  $\sigma_c$  can be reasonably constrained with the galaxy clustering measurements, where they estimated  $\sigma_c$  for the BOSS CMASS galaxies to be around  $0.18$ , consistent with that of [Yang et al. \(2012\)](#). In this paper, we simply set the intrinsic scatter  $\sigma_c$  to be a constant of  $0.173$  in the redshift range of  $0.1 < z < 0.8$ . We will discuss the effect of different  $\sigma_c$  values in Section 6.

The function  $\langle M_*|M \rangle$  is the average central galaxy stellar mass in halos of mass  $M$ . We adopt a broken power law relation as in [Yang et al. \(2012\)](#) (see also [Moster et al. 2010, 2013](#)),

$$\langle M_*|M \rangle = M_{*,0} \frac{(M/M_1)^{\alpha+\beta}}{(1+M/M_1)^\beta} \quad (11)$$

where  $M_{*,0}$ ,  $M_1$ ,  $\alpha$ , and  $\beta$  are the four free parameters in this relation. The values of  $\alpha + \beta$  and  $\alpha$  are the low and high-mass end slopes of the SHMR, respectively.

To properly estimate the missing fraction of galaxies in the BOSS observation, [Leauthaud et al. \(2016\)](#) derived the stellar mass completeness by comparing the observed (incomplete) BOSS galaxy SMFs with the total SMFs obtained by combining the measurements of PRIMUS

<sup>5</sup> <https://www.cosmosim.org/cms/simulations/bigmdpl/>

and deeper imaging of the stripe 82 region (Bundy et al. 2015). They found that the stellar mass completeness of BOSS galaxies at different redshifts can be well described by the following functional form,

$$c(M_*) = \frac{f}{2} \left[ 1 + \operatorname{erf} \left( \frac{\log M_* - \log M_{*,\min}}{\sigma} \right) \right], \quad (12)$$

where erf is the error function and the free parameters are  $f$ ,  $M_{*,\min}$  and  $\sigma$ . This relation allows for the massive-end stellar mass completeness,  $f$ , to be less than unity to take into account the possibility of missing very massive galaxies. The parameter  $M_{*,\min}$  sets the stellar mass scale where on average  $f/2$  of the galaxies are selected. This probe using the SMF measurements from other volume-limited samples provides a simple and straightforward way to roughly estimate the stellar mass completeness. However, as the completeness factor is constrained from small-area deep surveys, one can not take advantage of measuring accurate stellar mass functions from a very large survey, which are less impacted by the cosmic variance.

Since the central and satellite galaxies have quite different color distributions (e.g., Yang et al. 2017), the color selection criteria in the BOSS observation may thus result in different incompleteness effects between central and satellite galaxies. Therefore, we adopt different sets of free parameters in Eq. 12 for central and satellite galaxies. That is, we have in total six free parameters to describe the incompleteness functions, three parameters ( $f_{\text{I}}$ ,  $M_{*,\min,\text{I}}$  and  $\sigma_{\text{I}}$ ) for central galaxies  $c_{\text{I}}(M_*)$  and three parameters ( $f_{\text{II}}$ ,  $M_{*,\min,\text{II}}$  and  $\sigma_{\text{II}}$ ) for satellite galaxies,  $c_{\text{II}}(M_*)$ .

The incomplete occupation function of central and satellite galaxies, i.e., the average number of *observed* central and satellite galaxies with stellar mass  $M_{*,1} < M_* < M_{*,2}$  in halos of mass  $M$  can be estimated as (Yang et al. 2012)

$$\langle N_{\text{C}}(M) \rangle = \int_{M_{*,1}}^{M_{*,2}} \Phi_{\text{C}}(M_*|M) c_{\text{I}}(M_*) dM_* \quad (13)$$

$$\langle N_{\text{S}}(M) \rangle = \int_{M_{*,1}}^{M_{*,2}} \Phi_{\text{S}}(M_*|M) c_{\text{II}}(M_*) dM_*, \quad (14)$$

where  $\Phi_{\text{S}}(M_*|M)$  is the CSMF for the satellite galaxies. We assume that satellite galaxies have the same CSMF as the centrals when they are distinct halos at the last accretion epoch, as widely used in the subhalo abundance matching algorithm (see Yang et al. 2017, and references therein). Then the total satellite galaxy distribution in halos of mass  $M$  can be described as,

$$\Phi_{\text{S}}(M_*|M) = \int dM_{\text{acc}} \Phi_{\text{C}}(M_*|M_{\text{acc}}) n_{\text{S}}(M_{\text{acc}}|M), \quad (15)$$

where  $M_{\text{acc}}$  is the subhalo mass at the last accretion epoch and  $n_{\text{S}}(M_{\text{acc}}|M)$  is the corresponding subhalo mass function in host halos of mass  $M$ .

Note that within this framework, we have assumed the same SHMR for central and satellite galaxies, which is not exactly true. We have ignored the possible evolution of CSMF between the accretion epoch and the redshift of interest. We also ignore the growth and tidal stripping effects for the satellite galaxy stellar mass after accretion.

As found by recent studies of Guo et al. (2016) and Yang et al. (2017), the central and satellite galaxies tend to have somewhat different galaxy-halo relations. As shown in Figure 2 of Guo et al. (2016), the projected 2PCF  $w_{\text{p}}(r_{\text{p}})$  would be underestimated when using  $M_{\text{acc}}$  as the subhalo mass by assuming the same SHMR as the central galaxies. The agreement with the observed  $w_{\text{p}}(r_{\text{p}})$  can be improved by adopting different SHMRs for central and satellite galaxies (Figure 6 in Guo et al. 2016).

In general, one may assume different SHMRs for central and satellite galaxies, and use the observed  $w_{\text{p}}(r_{\text{p}})$  and SMFs to make constraints on both of them. However, assuming different SHMRs for satellite galaxies will introduce another four free parameters ( $M_{*,0}$ ,  $M_1$ ,  $\alpha$ , and  $\beta$ ). Since the SHMRs of the central and satellite galaxies are not completely independent, the observation would be over-fitted by adopting completely independent SHMRs for central and satellite galaxies. A more consistent and reasonable model is to include the redshift evolution in the central galaxy SHMR and the stellar mass evolution of satellite galaxies after accretion, as those carried out in Yang et al. (2012). We will defer such a sophisticated model of galaxy stellar mass evolution based on BOSS observation in a subsequent paper. Although we are not modeling the evolutionary trajectories of satellite galaxies, these effects only have minimal influence on the total SMF as the majority of galaxies in these massive galaxy samples are central galaxies (White et al. 2011; Parejko et al. 2013; Guo et al. 2014). In addition, as these effects might compromise at certain levels, the SHMRs obtained from central and satellite galaxies are still quite similar (Yang et al. 2017).

In practice, since we are using halos/subhalos from simulations for our study, the satellite occupation function in subhalos of mass  $M_{\text{acc}}$  can be directly estimated as,

$$\langle N_{\text{S}}(M_{\text{acc}}) \rangle = \int_{M_{*,1}}^{M_{*,2}} \Phi_{\text{C}}(M_*|M_{\text{acc}}) c_{\text{II}}(M_*) dM_*. \quad (16)$$

With these HOD definitions, we can then split the galaxy sample into different stellar mass ranges, and calculate the clustering measurements for these subsamples to constrain the ICSMF model parameters as in Yang et al. (2012). We note that the effect of  $\sigma_{\text{c}}$  on the galaxy clustering is automatically taken into account in Eqs. 13 and 16.

### 3.1.2. Two-point Correlation Function and Stellar Mass Function

With the ICSMF for central and satellite galaxies, we measure the galaxy 2PCF by applying the simulation-based method of Zheng & Guo (2016) with the halo catalogs in the BigMDPL simulations, which overcomes the difficulty of modeling the halo exclusion effect, the scale-dependent halo bias, and the residual redshift-space distortion effect. By tabulating the clustering measurements of the halos and subhalos, this method is equivalent to, but significantly more efficient than, directly populating halos and subhalos in the simulations with galaxies using the occupation function,  $\langle N_{\text{C}}(M) \rangle$  and  $\langle N_{\text{S}}(M_{\text{acc}}) \rangle$ . In detail, The 3D galaxy 2PCF  $\xi(\mathbf{r})$  is measured in the BigMDPL simulations as follows (Zheng &

Guo 2016),

$$\begin{aligned} \xi(\mathbf{r}) = & \sum_{i,j} \frac{n_{h,i} n_{h,j}}{\bar{n}_g^2} \langle N_c(M_i) \rangle \langle N_c(M_j) \rangle \xi_{hh}(\mathbf{r}; M_i, M_j) \\ & + \sum_{i,j} 2 \frac{n_{h,i} n_{s,j}}{\bar{n}_g^2} \langle N_c(M_i) \rangle \langle N_s(M_{acc,j}) \rangle \xi_{hs}(\mathbf{r}; M_i, M_{acc,j}) \\ & + \sum_{i,j} \frac{n_{s,i} n_{s,j}}{\bar{n}_g^2} \langle N_s(M_{acc,i}) \rangle \langle N_s(M_{acc,j}) \rangle \xi_{ss}(\mathbf{r}; M_{acc,i}, M_{acc,j}) \end{aligned} \quad (17)$$

where  $n_h(M)$  and  $n_s(M_{acc})$  are the halo mass function and subhalo mass function at the last accretion epoch, respectively. The predicted galaxy number density  $\bar{n}_g$  can be calculated as,

$$\bar{n}_g = \sum_i [\langle N_c(M_i) \rangle n_h(M_i) + \langle N_s(M_{acc,i}) \rangle n_s(M_{acc,i})]. \quad (18)$$

The 3D 2PCFs  $\xi_{hh}(\mathbf{r}; M_i, M_j)$ ,  $\xi_{hs}(\mathbf{r}; M_i, M_{acc,j})$ , and  $\xi_{ss}(\mathbf{r}; M_{acc,i}, M_{acc,j})$  are the tabulated 2PCFs of the halo-halo, halo-subhalo, and subhalo-subhalo pairs between the different mass bins from the simulation. With the help of halo and subhalo catalogs, we can accurately measure  $\xi(\mathbf{r}; M_i, M_j)$  directly from the simulations, rather than applying any theoretical models for the halo bias  $b_h(M)$  (Mo et al. 1996).

To reduce the effect of redshift-space distortion (RSD) caused by galaxy peculiar velocities, we focus on the measurements of the projected 2PCF  $w_p(r_p)$  (Davis & Peebles 1983), defined as,

$$w_p(r_p) = 2 \int_0^{r_{\pi, \max}} \xi(r_p, r_\pi) dr_\pi, \quad (19)$$

where  $r_\pi$  and  $r_p$  are the separations of galaxy pairs along and perpendicular to the line-of-sight (LOS).  $r_{\pi, \max}$  is the maximum LOS distance to achieve the best signal-to-noise ratio.

The observed (incomplete) galaxy SMF of the BOSS sample can be predicted as,

$$\begin{aligned} \Phi(M_*) = & \int dM \Phi_c(M_*|M) c_{\text{I}}(M_*) n_h(M) \\ & + \int dM_{\text{acc}} \Phi_c(M_*|M_{\text{acc}}) c_{\text{II}}(M_*) n_s(M_{\text{acc}}) \end{aligned} \quad (20)$$

In summary, we have four free parameters ( $M_{*,0}$ ,  $M_1$ ,  $\alpha$ , and  $\beta$ ) for the stellar-halo mass relation (Eq. 11) and another six parameters ( $f_{\text{I}}$ ,  $M_{*,\text{min,I}}$ ,  $\sigma_{\text{I}}$ ,  $f_{\text{II}}$ ,  $M_{*,\text{min,II}}$  and  $\sigma_{\text{II}}$ ) for the incompleteness component (Eq. 12). The predictions of  $\Phi(M_*)$  and  $w_p(r_p)$  can then be compared with those measured in the observed galaxy sample in order to constrain the best-fitting model parameters.

With the best-fitting model parameters, we can infer the intrinsic galaxy total SMF  $\tilde{\Phi}(M_*)$  at each redshift interval as,

$$\begin{aligned} \tilde{\Phi}(M_*) = & \int dM \Phi_c(M_*|M) n_h(M) \\ & + \int dM_{\text{acc}} \Phi_c(M_*|M_{\text{acc}}) n_s(M_{\text{acc}}). \end{aligned} \quad (21)$$

### 3.2. Observational Measurements

With the above listed models for the galaxy projected 2PCFs and SMFs, we can use the related observational measurements to constrain the model parameters.

We measure the projected 2PCF  $w_p(r_p)$  for BOSS galaxies through the Landy–Szalay estimator (Landy & Szalay 1993). In practice, we integrate  $\xi(r_p, r_\pi)$  in Eq. (19) to a maximum LOS distance of  $r_{\pi, \max} = 100 h^{-1} \text{Mpc}$  to achieve the best signal-to-noise ratio, and the same value is adopted in the model calculation. We choose logarithmic  $r_p$  bins with a width  $\Delta \log r_p = 0.2$  from 1 to  $63.1 h^{-1} \text{Mpc}$ , and linear  $r_\pi$  bins of width  $\Delta r_\pi = 2 h^{-1} \text{Mpc}$  from 0 to  $100 h^{-1} \text{Mpc}$ . We measure the projected 2PCFs for the two stellar mass ranges of  $10^{11} M_\odot < M_* < 10^{11.5} M_\odot$  and  $10^{11.5} M_\odot < M_* < 10^{12} M_\odot$ .

The observed galaxy SMF is measured for galaxy stellar mass in the range of  $10^{11}$  to  $10^{12} M_\odot$  with a logarithmic width of  $\Delta \log M_* = 0.1$ . Therefore, we have 28 data points in total, with 18 for  $w_p(r_p)$  and 10 for  $\Phi(M_*)$ . We estimate the error covariance matrices for  $w_p(r_p)$  and  $\Phi(M_*)$  using the jackknife re-sampling technique with 100 subsamples (Guo et al. 2013, 2014). We note that the cross-covariance between the  $w_p(r_p)$  measurements for the two stellar mass bins are also taken into account in the covariance matrix. The jackknife re-sampling method provides a reasonable way to estimate the sample variance effect (see agreement with the errors estimated from mock catalogs in the Appendix B of Guo et al. 2013).

### 3.3. Model Constraints

In order to fully explore the probability distribution of the model parameters, we apply a Markov Chain Monte Carlo (MCMC) method. The likelihood surface is determined by  $\chi^2$ , contributed by the observed galaxy stellar mass function  $\Phi(M_*)$  and the projected 2PCF  $w_p(r_p)$ ,

$$\chi^2 = \chi_{w_p}^2 + \frac{(\Phi - \Phi^*)^2}{\sigma_\Phi^2} \quad (22)$$

$$\chi_{w_p}^2 = (\mathbf{w}_p - \mathbf{w}_p^*)^T \mathbf{C}_{w_p}^{-1} (\mathbf{w}_p - \mathbf{w}_p^*), \quad (23)$$

where  $\mathbf{C}_{w_p}$  is the full error covariance matrix of  $w_p(r_p)$ . The quantity with (without) a superscript ‘\*’ is the one from the data (model). The degree of freedom (dof) of the model is 18, i.e., dof = 28 – 10.

Here we only adopt the diagonal elements of the covariance matrix of  $\Phi$ , because the uncertainties from systematic effects of stellar mass measurements are hard to estimate (Mitchell et al. 2013). The contribution of Poisson noise to the observed SMF is added in quadrature to  $\sigma_\Phi$ .

## 4. TEST THE PERFORMANCE OF OUR METHOD

### 4.1. Tests with mock catalogs

Before we apply our method to the BOSS galaxies, we perform a validity test on a mock galaxy catalog in the redshift range of  $0.1 < z < 0.2$  that has the same geometry as the BOSS sample. We first assign each halo in the BigMDPL simulation a value of galaxy stellar mass according to the following model parameters of Eq. 11,

$$\log M_{*,0} = 10.459, \log M_1 = 10.844, \alpha = 0.309, \beta = 8.077,$$

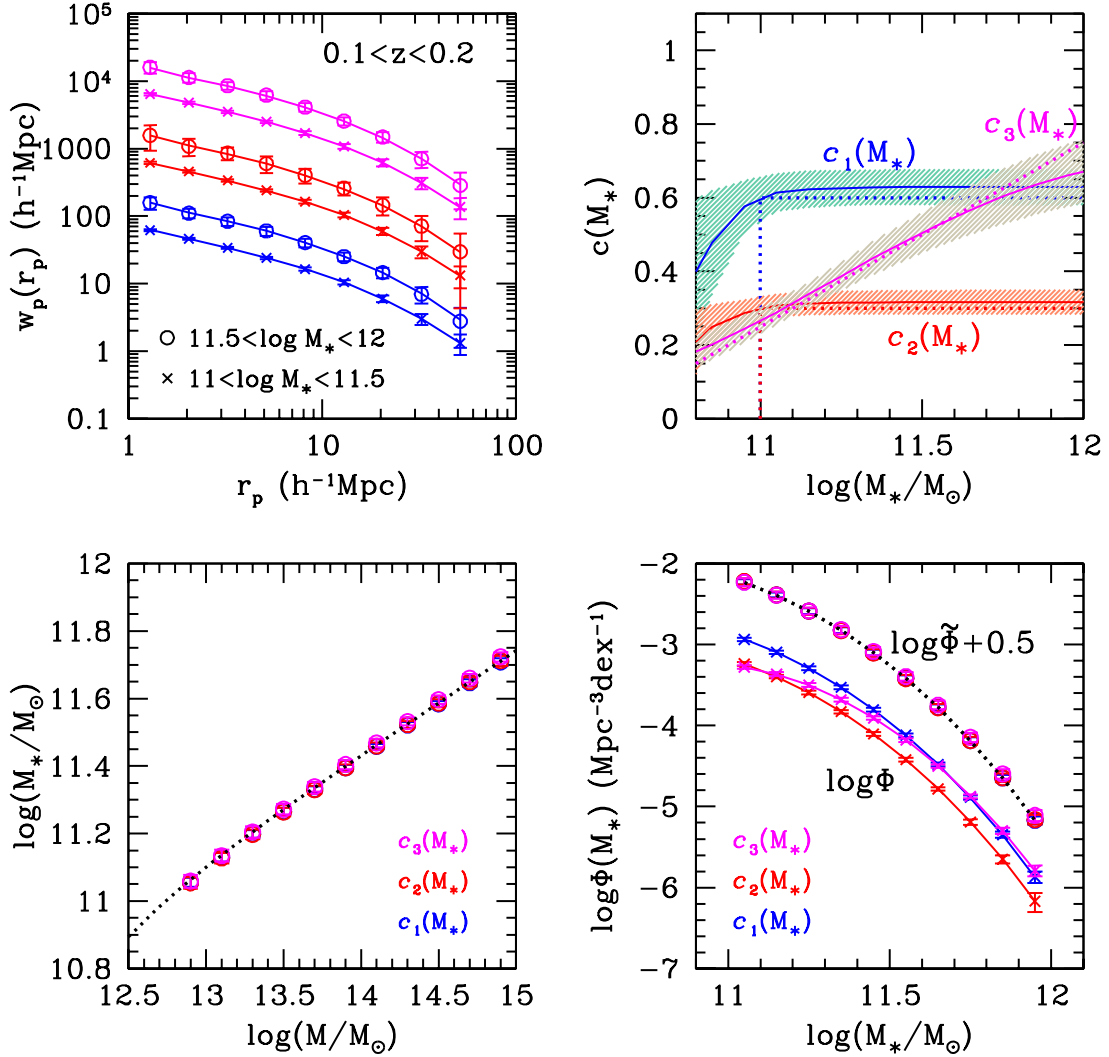


FIG. 3.— Tests of our method using mock galaxy catalogs. We constructed three mock catalogs with different selection functions of Eqs. 24, 25 and 26, displayed as the blue, red, and magenta symbols (and lines), respectively. Top Left: measurements of  $w_p(r_p)$  with the circles and crosses for the stellar mass ranges of  $10^{11}–10^{11.5}M_\odot$  and  $10^{11.5}–10^{12}M_\odot$ , respectively. The measurements for the  $c_2(M_*)$  and  $c_3(M_*)$  models are shifted upward by 1 dex and 2 dex for clarity, respectively. The best-fitting models are shown as the solid lines. Top Right: the three different selection functions, with the dotted lines as the input models and the solid lines with shaded regions as the median and  $1\sigma$  uncertainties of the best-fitting models. Bottom Left: comparisons of the stellar-halo mass relations, with the circles for the best-fitting models and the dotted line for the input model. Bottom Right: the observed and total galaxy SMFs, with the crosses for the observed galaxy SMFs  $\Phi(M_*)$  and the circles for the predicted total SMFs  $\tilde{\Phi}(M_*)$  from the best-fitting models. The solid lines are the best-fitting models for  $\Phi(M_*)$ . The black dotted line is for the input model of  $\tilde{\Phi}(M_*)$ . The measurements for  $\tilde{\Phi}(M_*)$  are shifted upward by 0.5 dex for clarity.

which are adopted from Yang et al. (2012) as the best-fitting parameters at the simulation output redshift of  $z = 0.152$  (see Yang et al. 2012, for more parameters for different sets of cosmologies). We note that satellite galaxies are included in the mock catalogs by applying the SHMR with the subhalo mass at the accretion epoch. Once the dark matter halos and subhalos are populated with galaxies of different stellar masses, we then place a virtual observer at the center of the simulation volume and calculate the right ascension, declination and redshift for each galaxy. The galaxy peculiar velocity is taken into account when calculating the redshift.

We first test our method for the case of the same stellar mass completeness function  $c(M_*)$  for central and satellite galaxies, i.e.,  $c_I(M_*) = c_{II}(M_*)$ . We constructed three mock catalogs by applying the following three sim-

ple selection models on the central and satellite galaxies,

$$c_1(M_*) = 0.6, \quad (24)$$

$$c_2(M_*) = 0.3, \quad (25)$$

$$c_3(M_*) = (\log M_* - 10.5)/2, \quad (26)$$

The models  $c_1(M_*)$  and  $c_2(M_*)$  are random selections with different rates. The model  $c_3(M_*)$  is a linear selection with higher rates for more massive galaxies.

We then measure  $w_p(r_p)$  and  $\Phi(M_*)$  for these mock catalogs and run the MCMC chains to find the best-fitting model parameters. The results are displayed in Figure 3, with the blue, red and magenta symbols (and lines) for the three mock catalogs with  $c_1(M_*)$ ,  $c_2(M_*)$  and  $c_3(M_*)$ , respectively. The top left panel shows the projected 2PCFs  $w_p(r_p)$ , with the crosses and circles for the stellar mass ranges of  $10^{11}–10^{11.5}M_\odot$  and  $10^{11.5}–$

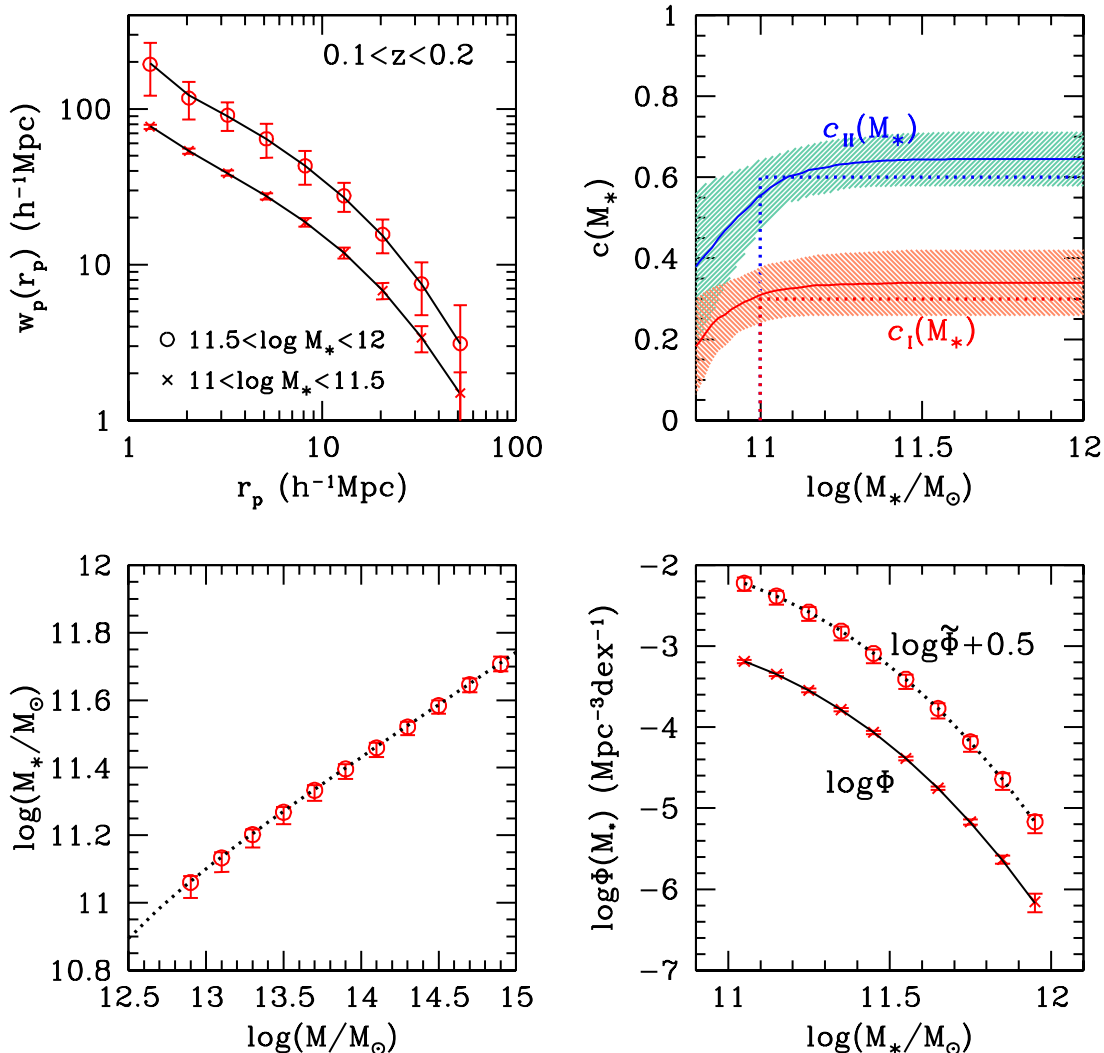


FIG. 4.— Similar to Figure 3, but for the case of different completeness functions for central and satellite galaxies, i.e.,  $c_I(M_*) = 0.3$  and  $c_{II}(M_*) = 0.6$ .

$10^{12}M_\odot$ , respectively. For clarity, the measurements for the  $c_2(M_*)$  and  $c_3(M_*)$  models are shifted upward by 1 dex and 2 dex, respectively. The completeness functions are shown in the top right panel, where the dotted lines are for the input models and the solid lines with shaded regions are the average of the best-fitting models with  $1\sigma$  uncertainties. As can be seen, the fiducial  $c(M_*)$  are very nicely recovered for all the three different selection models. As we only use galaxies with stellar masses larger than  $10^{11}M_\odot$  for both  $w_p(r_p)$  and  $\Phi(M_*)$ , the discrepancies shown for  $M_* < 10^{11}M_\odot$  do not have any effect on the results.

The stellar-halo mass relations from the best-fitting models are shown as the circles in the bottom left panel, where the dotted line is the input model. The input model parameters are also very well recovered from the best-fitting models. The observed galaxy SMFs are shown as the crosses with different colors in the bottom right panel, where the best-fitting models are shown as the solid lines. The predicted galaxy total SMFs from the best-fitting models are displayed as the circles, which are shifted upward by 0.5 dex for clarity. The fiducial model (black dotted line) is successfully recovered from

our best-fitting models.

Before we apply our ICSMF model to the BOSS observation, it is important to check to what extent the true incompletenesses for central and satellite galaxies can be recovered if they are different. To this end, we input  $c_I(M_*) = 0.3$  for central galaxies,  $c_{II}(M_*) = 0.6$  for satellite galaxies, and perform the same procedure above. As shown in Figure 4, both the input completeness functions, the SHMR, as well as the total galaxy SMF are very well recovered, demonstrating the validity of our ICSMF model to accurately predict the galaxy SMFs from incomplete samples with complicated target selections. In the following sections, we will use separate completeness functions for central and satellite galaxies to model the real BOSS galaxy samples.

#### 4.2. Test with BOSS LOWZ galaxy sample

As the BOSS LOWZ galaxy sample also covers the redshift range of  $0.1 < z < 0.2$ , where accurate galaxy SMFs have been measured in literature using the SDSS DR7 Main galaxy sample. As a consistency check, we also apply our method to the BOSS galaxies in this redshift range and compare with literature.

We show in Figure 5 the modeling results for the



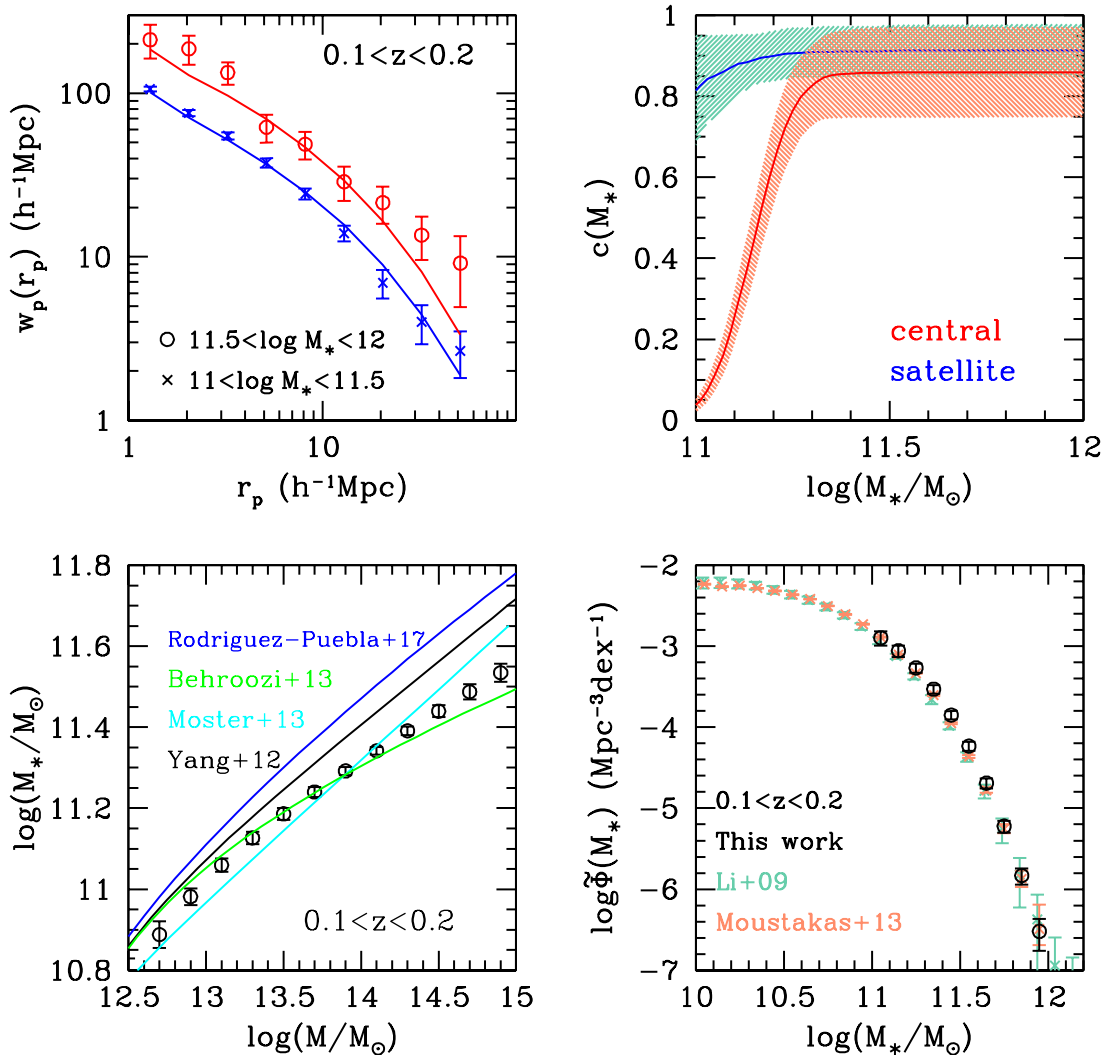


FIG. 5.— Similar to Figure 3, but for the BOSS galaxies at  $0.1 < z < 0.2$ . We show the SHMR of our best-fitting model as the circles in the bottom left panel. In comparisons, those of Yang et al. (2012), Moster et al. (2013), Behroozi et al. (2013a) and Rodríguez-Puebla et al. (2017) are shown as lines of different colors. In the bottom right panel, we compare our measurement of the galaxy total SMF (circles) with those obtained by Li & White (2009) and Moustakas et al. (2013) (crosses with different colors)

$w_p(r_p)$  (top left panel),  $c(M_*)$  (top right panel), SHMR (bottom left panel), and the total galaxy SMF (bottom right panel) at  $0.1 < z < 0.2$  as in Figure 3. The low-redshift sample of BOSS is more than 85% complete for  $M_* > 10^{11.4}M_\odot$ .

In the bottom left panel, we compare the SHMR for our best-fitting model (circles) with the predictions of different theoretical models of Yang et al. (2012), Behroozi et al. (2013a), Moster et al. (2013), and Rodríguez-Puebla et al. (2017) (lines of different colors). The high-mass end slope of the SHMR is not well constrained in previous literature, where significant differences exist among the models. These differences mainly come from three origins: (1) the stellar mass functions in these studies are somewhat different; (2) the cosmological parameters adopted are different; (3) the scatter  $\sigma_c$  used in these studies are somewhat different as well. Our measurements here agree best with the model of Behroozi et al. (2013a) at this redshift interval.

Our predicted galaxy total SMF from the BOSS sample is shown as the black circles in the bottom right panel. We also compare them with the galaxy SMFs measured

in Li & White (2009) using SDSS DR7 and Moustakas et al. (2013) using the joint sample of SDSS and Galaxy Evolution Explorer (GALEX; Martin et al. 2005). We use the stellar mass measurements estimated with the  $r$ -band model magnitude from Li & White (2009) to account for the fact that the typical  $r$ -band Petrosian magnitudes would result in the underestimation of the galaxy stellar mass (Guo et al. 2010). We add a constant offset of  $-0.05$  dex to the stellar mass of the Moustakas et al. (2013) to account for the Flexible Stellar Population Synthesis (FSPS) models used in their stellar mass estimates (see their Figure 19 for comparisons of different SPS models). We find very good agreement between our measurements and those from the literature.

The above two sets of tests demonstrate that our method is robust in recovering the missing fraction of galaxies, as well as providing unbiased measurements of the galaxy SMFs and SHMRs from large-scale surveys with complicated target selections. In the following sections, we will apply our method to the BOSS galaxies in  $0.2 < z < 0.8$  to predict the galaxy total SMFs and SHMRs.

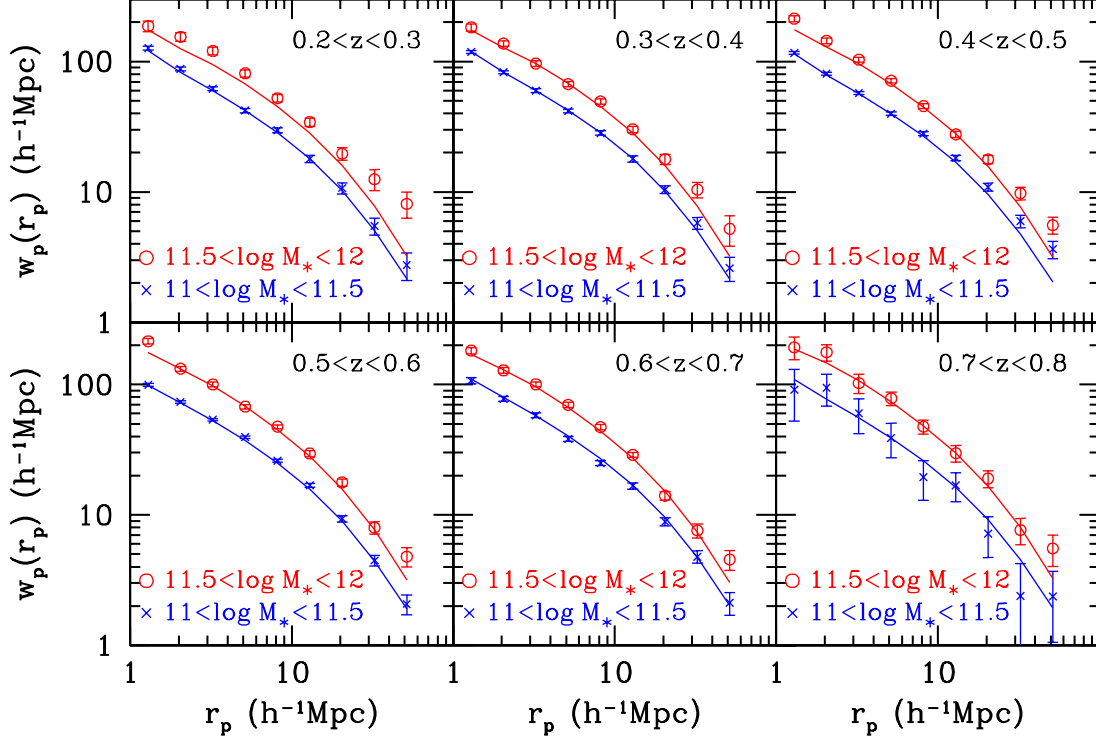


FIG. 6.— Projected 2PCFs for the BOSS galaxies at redshifts from 0.2 to 0.8. The blue and red symbols are for the stellar mass ranges of  $10^{11}$ – $10^{11.5}M_{\odot}$  and  $10^{11.5}$ – $10^{12}M_{\odot}$ , respectively. The solid lines are our best-fitting models.

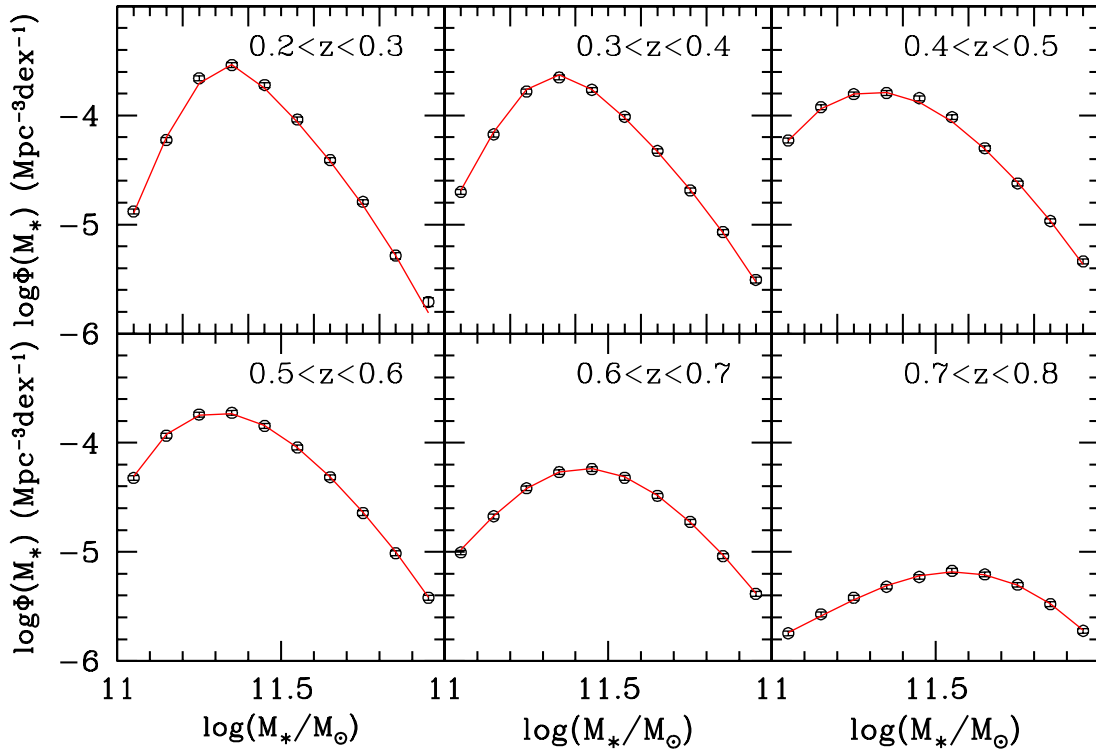


FIG. 7.— Observed galaxy SMF (circles with errors),  $\Phi(M_*)$ , in units of  $\text{Mpc}^{-3}\text{dex}^{-1}$ , in different redshift ranges from  $z = 0.2$  to 0.8. The solid lines are our best-fitting models.

## 5. RESULTS

## 5.1. ICSMF model constraints

We measure the projected 2PCFs and the incomplete SMFs from BOSS observation within redshift range of  $0.2 < z < 0.8$  according to the methods outlined in section 3.2. Here galaxies are divided into different samples according to the criteria listed in Table 1. These measurements are then used to constrain the ICSMF model parameters using the algorithm outlined in section 3.3.

We show in Figure 6 the projected 2PCF measurements for the BOSS galaxies at  $0.2 < z < 0.8$ . The blue and red symbols are for galaxies in the stellar mass ranges of  $10^{11} - 10^{11.5} M_{\odot}$  and  $10^{11.5} - 10^{12} M_{\odot}$ , respectively. Our best-fitting models are shown as the solid lines of different colors. The clustering amplitude of  $w_p(r_p)$  for the more massive sample is about twice that of the lower mass sample, which is consistent with the galaxy bias measurements of Tinker et al. (2017). As these BOSS galaxies generally live in halos of masses larger than  $10^{12} M_{\odot}$ , the halo bias is quickly increasing with mass for these massive halos (Mo et al. 1996; Tinker et al. 2005). Our best-fitting models reasonably fit all the observed  $w_p(r_p)$ , except for the high mass sample at  $0.2 < z < 0.3$ . While the best-fitting  $\chi^2$  (41.7) for this sample is still reasonable for a degree-of-freedom of 18, the slight deviation is possibly related to the assumption of the same SHMR for central and satellite galaxies and the constant scatter  $\sigma_c$ . The current BOSS measurements are not accurate enough to fully constrain those sophisticated models with more freedom.

Figure 7 shows our best-fitting models for the observed galaxy SMFs at different redshifts, with the circles for the measured galaxy SMFs in BOSS and solid lines for our best-fitting models. The agreement between the data and models for galaxy samples at different redshifts are remarkably good, implying that the sample selection functional forms used in this study are suitable.

The best-fitting stellar mass completeness functions for the different galaxy samples are shown in Figure 8, with the red and blue solid lines for central and satellite galaxies, respectively. The shaded area represent the model uncertainties. The BOSS galaxy samples are more than 80% complete for massive galaxies of  $M > 10^{11.5} M_{\odot}$  at  $z < 0.6$ , but the completeness decreases very fast for lower mass galaxies, causing the galaxy SMF to decrease at the low mass end in Figure 7. At higher redshifts of  $z > 0.7$ , even those very massive galaxies are only about 30% complete. For comparison, we also display the completeness estimates from Leauthaud et al. (2016) as the circles in the redshift range of  $0.2 < z < 0.7$ . As their estimates are for the whole BOSS sample, they are more comparable to the completeness functions of our central galaxies, because the central galaxies dominate the BOSS sample. Our predictions are generally in good agreement with their estimates at all redshifts.

The completeness of satellite galaxies at the massive end,  $f_{II}$ , is not as well constrained as that of central galaxies, as seen from the  $1\sigma$  distribution. It is related to the fact that central galaxies dominate the massive end of the SMF (Yang et al. 2009). But at the low mass end, the completeness of satellite galaxies is quite well constrained and generally larger than that of the central galaxies. It is caused by the  $i$ -band sliding cut

( $i < 19.86 + 1.6(d_{\perp} - 0.8)$ ) of the BOSS CMASS target selections to remove the fainter and bluer galaxies (see e.g., Figure 1 of Guo et al. 2013), while the low-mass red galaxies have higher satellite fractions (see e.g., Zehavi et al. 2011; Guo et al. 2014; Saito et al. 2016; Yang et al. 2017). Therefore, the color selection of the BOSS galaxies samples at a given stellar mass is also taken into account in our separate modeling of the completeness functions for the central and satellite galaxies.

## 5.2. Central Galaxy Stellar-Halo Mass Relation

We show in Figure 9 the best-fitting central galaxy SHMRs for the different redshift samples (circles with errors), in comparison to five other different theoretical models of Leauthaud et al. (2012), Yang et al. (2012), Behroozi et al. (2013a), Moster et al. (2013), and Rodríguez-Puebla et al. (2017) (lines of different colors). For fair comparisons, we have corrected the predicted halo masses for the different cosmologies used in these models. The halos in Leauthaud et al. (2012), Yang et al. (2012) and Moster et al. (2013) are defined as 200 times the background mass density, 180 times the background density and 200 times the critical density, respectively. We correct these definitions to our definition of the virial halo mass in the ROCKSTAR halo finder using the average offsets in the BigMDPL simulation. At  $z > 0.5$ , the halo definition of 200 times the background density is very similar to the virial mass definition, with a correction at the level of about 0.01 dex.

Generally, we find a steeper slope of the central galaxy SHMR for these massive galaxies at  $z > 0.3$ , compared to other models. In these previous models, the galaxy SHMR is generally derived by fitting models to a set of different observations of the galaxy SMFs, clustering measurements, or galaxy weak lensing measurements at different redshifts. Because of the different systematics and statistical errors in the estimated galaxy stellar masses, fitting one SHMR model to different galaxy survey data would possibly generate inconsistent estimates of the corresponding halo masses at different redshifts. Therefore, we expect the existence of reasonable systematic offsets, although we have largely corrected for the assumptions about the IMF, SPS model and the dust attenuation model following the various offset values suggested in Rodríguez-Puebla et al. (2017).

As the high-mass end galaxy SMF measurements would be significantly affected by the Malmquist bias, the shape of the galaxy SHMR may somewhat dependent on the assumption of  $\sigma_c$ . We will discuss the effect of different  $\sigma_c$  values in Section 6. We show in Table 2 the best-fitting model parameters. We note that the low-mass end slope  $\alpha + \beta$  is not well constrained by our samples as we are only using galaxies more massive than  $10^{11} M_{\odot}$ . The high-mass end slope  $\alpha$  varies from about 1/4 to 1/2 from  $z = 0.1$  to  $z = 0.8$ .

## 5.3. Total Galaxy Stellar Mass Functions

As we demonstrated in Figure 4, with the accurate modeling of the observed galaxy SMFs and 2PCFs, we are able to make accurate predictions of the total galaxy SMFs as well. Taking advantage of the large galaxy samples of BOSS, we show with black circles in Figure 10 the total SMFs for galaxies in different redshift bins. For ref-

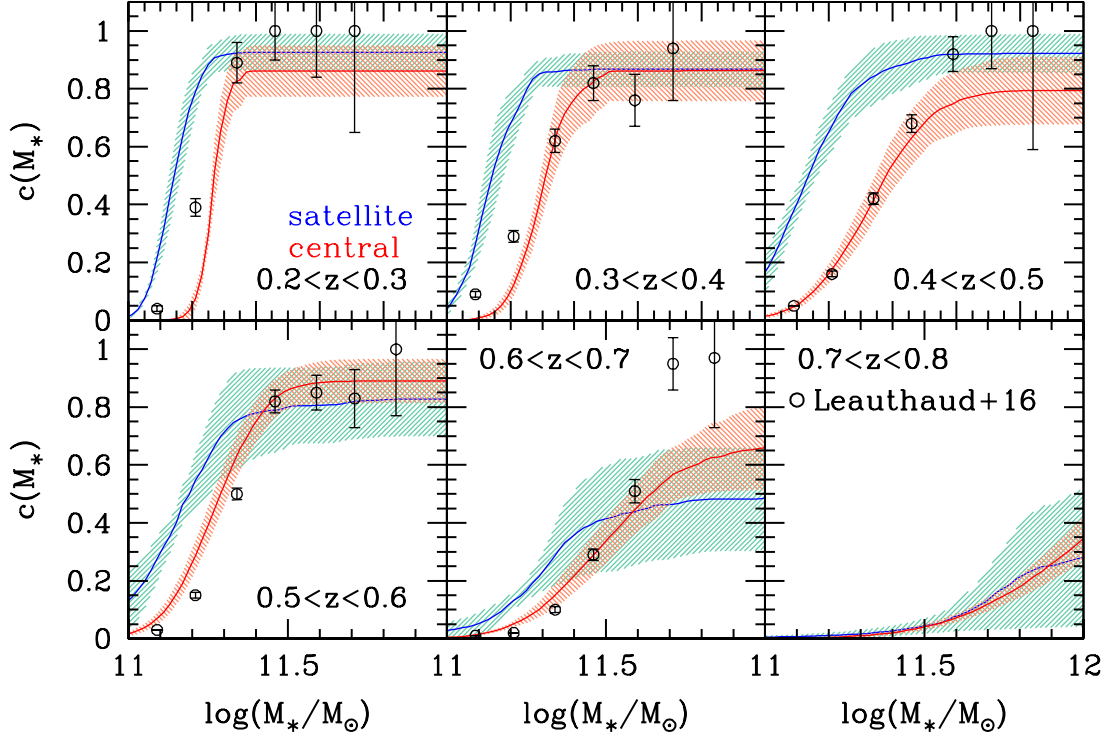


FIG. 8.— Stellar mass completeness functions for galaxies at different redshift ranges. The solid lines with the shaded area are the median and  $1\sigma$  uncertainties of the best-fitting models. The red and blue lines are for the central and satellite galaxies, respectively. The circles with errors are the estimates of the stellar mass completeness of all galaxies at  $0.2 < z < 0.7$  from [Leauthaud et al. \(2016\)](#).

TABLE 2  
BEST-FITTING MODEL PARAMETERS

Parameter	$0.1 < z < 0.2$	$0.2 < z < 0.3$	$0.3 < z < 0.4$	$0.4 < z < 0.5$	$0.5 < z < 0.6$	$0.6 < z < 0.7$	$0.7 < z < 0.8$
$\chi^2/\text{dof}$	19.96/18	41.76/18	13.92/18	44.01/18	34.91/18	21.75/18	10.20/18
$\log M_{*,0}$	$10.74^{+0.06}_{-0.20}$	$10.45^{+0.12}_{-0.01}$	$10.38^{+0.21}_{-0.22}$	$10.36^{+0.06}_{-0.17}$	$10.46^{+0.08}_{-0.23}$	$10.37^{+0.19}_{-0.22}$	$9.92^{+0.51}_{-0.06}$
$\log M_1$	$11.44^{+0.01}_{-0.42}$	$11.04^{+0.25}_{-0.01}$	$11.12^{+0.35}_{-0.39}$	$11.18^{+0.10}_{-0.28}$	$11.35^{+0.11}_{-0.33}$	$11.34^{+0.08}_{-0.27}$	$10.46^{+0.93}_{-0.08}$
$\alpha$	$0.23^{+0.03}_{-0.02}$	$0.33^{+0.02}_{-0.01}$	$0.38^{+0.01}_{-0.03}$	$0.42^{+0.02}_{-0.01}$	$0.41^{+0.03}_{-0.01}$	$0.47^{+0.02}_{-0.09}$	$0.48^{+0.05}_{-0.06}$
$\beta$	$7.89^{+0.46}_{-0.05}$	$8.00^{+0.06}_{-0.29}$	$8.25^{+0.24}_{-0.81}$	$8.49^{+0.06}_{-0.75}$	$7.49^{+0.89}_{-0.19}$	$7.30^{+1.18}_{-0.28}$	$8.13^{+0.41}_{-0.62}$
$f_I$	$0.94^{+0.03}_{-0.20}$	$0.93^{+0.02}_{-0.16}$	$0.93^{+0.04}_{-0.17}$	$0.82^{+0.09}_{-0.14}$	$0.87^{+0.09}_{-0.05}$	$0.51^{+0.37}_{-0.01}$	$0.53^{+0.38}_{-0.01}$
$\log M_{*,\text{min},I}$	$11.13^{+0.03}_{-0.01}$	$11.28^{+0.01}_{-0.03}$	$11.29^{+0.02}_{-0.01}$	$11.33^{+0.02}_{-0.02}$	$11.28^{+0.01}_{-0.04}$	$11.43^{+0.18}_{-0.02}$	$11.90^{+0.18}_{-0.01}$
$\sigma_I$	$0.11^{+0.02}_{-0.01}$	$0.07^{+0.01}_{-0.04}$	$0.11^{+0.02}_{-0.01}$	$0.23^{+0.01}_{-0.04}$	$0.21^{+0.01}_{-0.06}$	$0.23^{+0.13}_{-0.01}$	$0.39^{+0.11}_{-0.01}$
$f_{II}$	$0.94^{+0.03}_{-0.10}$	$0.99^{+0.01}_{-0.14}$	$0.96^{+0.01}_{-0.15}$	$0.97^{+0.02}_{-0.11}$	$0.96^{+0.01}_{-0.26}$	$0.55^{+0.11}_{-0.22}$	$0.23^{+0.36}_{-0.17}$
$\log M_{*,\text{min},II}$	$10.56^{+0.35}_{-0.09}$	$11.15^{+0.02}_{-0.03}$	$11.14^{+0.03}_{-0.04}$	$11.13^{+0.02}_{-0.04}$	$11.18^{+0.01}_{-0.08}$	$11.33^{+0.07}_{-0.07}$	$11.92^{+0.14}_{-0.47}$
$\sigma_{II}$	$0.30^{+0.12}_{-0.25}$	$0.09^{+0.02}_{-0.02}$	$0.12^{+0.02}_{-0.05}$	$0.17^{+0.09}_{-0.03}$	$0.13^{+0.06}_{-0.01}$	$0.36^{+0.06}_{-0.23}$	$0.68^{+0.17}_{-0.47}$

All masses are in units of  $M_\odot$ .

TABLE 3  
PREDICTED GALAXY TOTAL STELLAR MASS FUNCTION

$\log M_*$	$0.1 < z < 0.2$	$0.2 < z < 0.3$	$0.3 < z < 0.4$	$0.4 < z < 0.5$	$0.5 < z < 0.6$	$0.6 < z < 0.7$	$0.7 < z < 0.8$
11.05	$126.74 \pm 25.14$	$118.66 \pm 14.11$	$113.83 \pm 31.19$	$105.17 \pm 21.82$	$88.33 \pm 19.54$	$90.58 \pm 19.90$	$118.94 \pm 55.09$
11.15	$87.78 \pm 13.93$	$87.23 \pm 8.43$	$82.83 \pm 18.89$	$76.16 \pm 13.97$	$65.19 \pm 11.49$	$68.67 \pm 14.17$	$84.21 \pm 34.97$
11.25	$53.95 \pm 6.89$	$57.15 \pm 4.76$	$56.39 \pm 9.29$	$52.94 \pm 8.51$	$45.35 \pm 5.97$	$49.68 \pm 10.37$	$56.86 \pm 20.52$
11.35	$29.46 \pm 3.42$	$35.58 \pm 3.47$	$35.01 \pm 4.69$	$34.40 \pm 5.40$	$29.62 \pm 2.99$	$33.07 \pm 6.20$	$36.63 \pm 11.51$
11.45	$14.11 \pm 1.69$	$19.94 \pm 2.08$	$20.40 \pm 2.24$	$20.82 \pm 2.81$	$18.00 \pm 1.53$	$20.90 \pm 3.60$	$22.35 \pm 5.98$
11.55	$5.84 \pm 0.75$	$10.03 \pm 1.11$	$10.94 \pm 1.18$	$11.69 \pm 1.47$	$10.16 \pm 0.91$	$12.30 \pm 2.03$	$12.77 \pm 2.86$
11.65	$2.04 \pm 0.28$	$4.61 \pm 0.55$	$5.41 \pm 0.66$	$6.06 \pm 0.77$	$5.34 \pm 0.47$	$6.69 \pm 1.10$	$6.86 \pm 1.34$
11.75	$0.60 \pm 0.09$	$1.87 \pm 0.24$	$2.48 \pm 0.34$	$2.86 \pm 0.42$	$2.54 \pm 0.23$	$3.30 \pm 0.51$	$3.45 \pm 0.64$
11.85	$0.15 \pm 0.03$	$0.67 \pm 0.09$	$1.01 \pm 0.14$	$1.23 \pm 0.21$	$1.09 \pm 0.10$	$1.56 \pm 0.31$	$1.65 \pm 0.34$
11.95	$0.03 \pm 0.01$	$0.20 \pm 0.03$	$0.37 \pm 0.06$	$0.48 \pm 0.10$	$0.42 \pm 0.04$	$0.65 \pm 0.17$	$0.69 \pm 0.16$

The stellar mass is in units of  $M_\odot$ . The stellar mass function measurements are in units of  $10^{-5} \text{Mpc}^{-3} \text{dex}^{-1}$ .

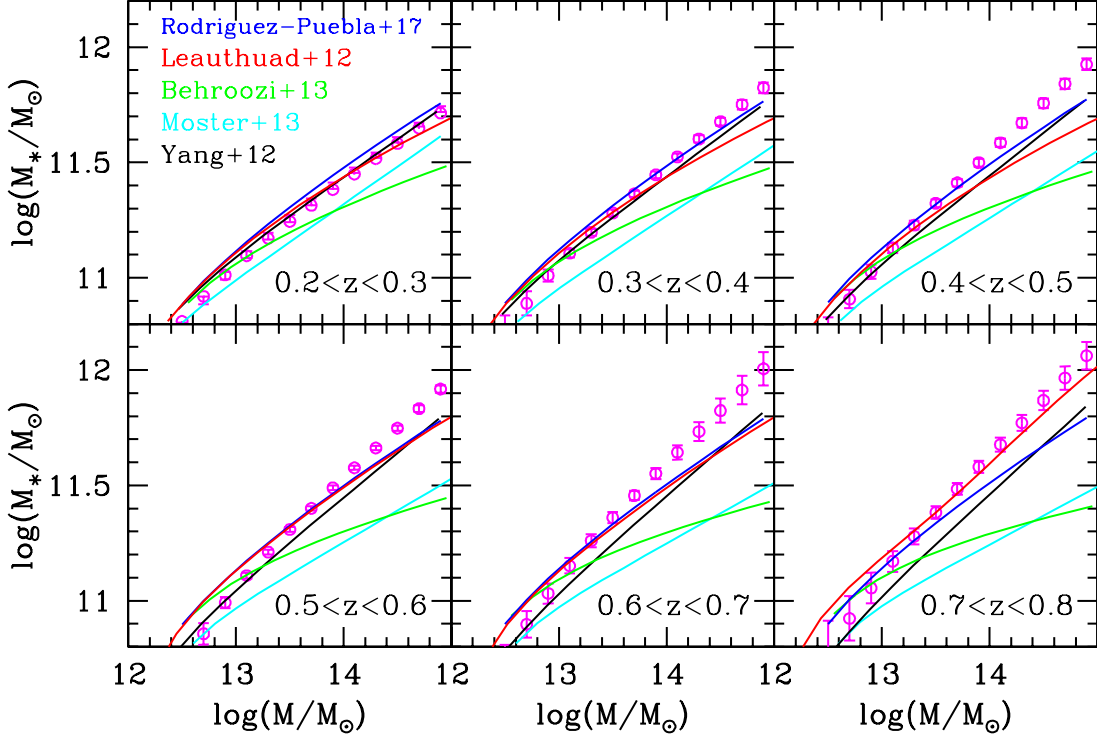


FIG. 9.— Comparisons of our best-fitting models of central galaxy SHMRs (circles with errors) to those of Leauthaud et al. (2012), Yang et al. (2012), Behroozi et al. (2013a), Moster et al. (2013), and Rodríguez-Puebla et al. (2017) (lines of different colors).

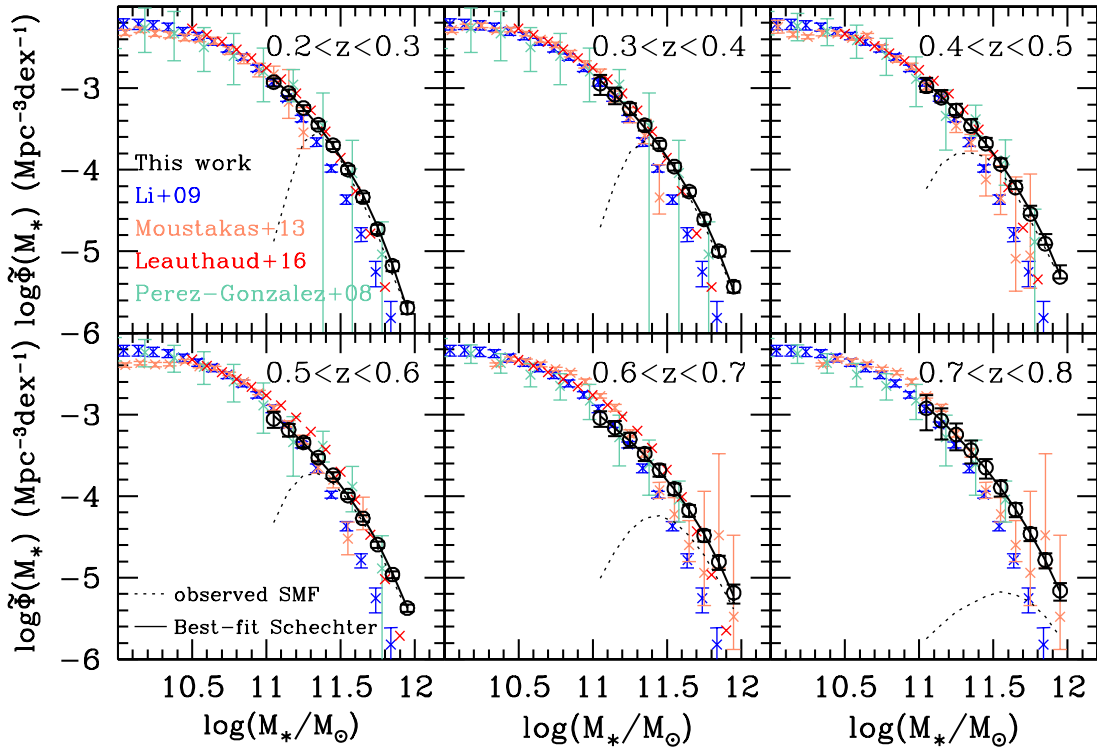


FIG. 10.— Total galaxy stellar mass functions,  $\tilde{\Phi}(M_*)$ , in different redshift bins. The black circles are our best-fitting models, while crosses of different colors represent the previous measurements of Pérez-González et al. (2008), Moustakas et al. (2013) and Leauthaud et al. (2016). We also show the measurements of Li & White (2009) at  $z \sim 0.1$  in each panel for comparison. We have corrected for the systematic offsets in the stellar mass estimates of Pérez-González et al. (2008) to be consistent with our measurements (see text). We note that the measurements of Pérez-González et al. (2008) are in bins of  $\Delta z = 0.2$ , so they are repeated in some neighboring bins. The measurements of Moustakas et al. (2013) at  $z > 0.5$  are in redshift bins of  $0.5 < z < 0.65$  and  $0.65 < z < 0.8$ . So we repeat their measurements of  $0.65 < z < 0.8$  for comparisons with our measurements at  $z > 0.6$ . The dotted and solid lines in each panel show the observed BOSS galaxy SMF and the best-fit Schechter function to the total SMF, respectively.

erence, the related values are listed in Table 3. The measurement errors have included the fractional errors of the observed galaxy SMFs in Figure 7, which are added in quadrature to the model uncertainties from the MCMC chains. For comparison, we also display the galaxy SMFs obtained by Pérez-González et al. (2008), Moustakas et al. (2013) and Leauthaud et al. (2016) in similar redshift ranges. The measurements of Li & White (2009) at  $z \sim 0.1$  are shown in each panel for easy comparison of the SMF evolution. The observed (uncorrected) BOSS galaxy SMF  $\Phi(M_*)$  is displayed as the dotted line in each panel. The measurements of Pérez-González et al. (2008) were obtained with the IMF of Salpeter (1955), the PEGASE SPS model (Fioc & Rocca-Volmerange 1997), and the dust model of Charlot & Fall (2000). As suggested by Bernardi et al. (2010) (their Table 2), we apply a correction of  $-0.22$  dex ( $-0.25$  dex for IMF and  $0.03$  dex for SPS model) to their stellar masses in order to be consistent with our measurements (see also Rodríguez-Puebla et al. 2017). We note that Rodríguez-Torres et al. (2016) also presented the expected total SMF for CMASS galaxies at  $0.55 < z < 0.65$  (their Figure 3). It was constructed by combining the observed CMASS SMF for  $M_* > 2.5 \times 10^{11} M_\odot$  and the SMF from Guo et al. (2010) for lower masses. Since we are using the same set of CMASS galaxies, we do not show it here.

The measurements of Pérez-González et al. (2008) (surveyed area  $\sim 0.184$  deg<sup>2</sup>), Moustakas et al. (2013) (surveyed area  $\sim 9$  deg<sup>2</sup>) and Leauthaud et al. (2016) (surveyed area  $\sim 139.4$  deg<sup>2</sup>) are limited by the small survey volumes and suffer from significant sample variance effects. From the comparisons, our SMF measurements are basically consistent with the trend seen in the previous ones, but we present the most accurate measurements for massive galaxies of  $M_* > 10^{11} M_\odot$ . At  $z > 0.6$  where significant differences between the SMF measurements appear in literature, our measurements tend to agree better with those of Pérez-González et al. (2008). Since the galaxy SMF measurements are generally used to infer the galaxy SHMR, it is therefore important to use the accurate galaxy SMFs to derive the galaxy SHMR at the massive end. Finally, we note that as the overall completeness for  $z > 0.7$  galaxy sample is very low in BOSS, we expect future larger surveys will obtain more accurate measurements of the galaxy total SMFs at these higher redshifts.

To ease comparisons with literature, we fit our measurements of the galaxy total SMF with a standard single Schechter function (Schechter 1976),

$$\Phi(M_*) = (\ln 10)\Phi^* \exp\left(-\frac{M_*}{M_c^*}\right) \left(\frac{M_*}{M_c^*}\right)^{1+\alpha^*} \quad (27)$$

The best-fit Schechter functions for the galaxy samples are shown as the solid lines in Figure 10. The best-fit parameters  $\Phi^*$ ,  $M_c^*$  and  $\alpha^*$  are displayed in Table 4. The low-mass end slope  $\alpha^*$  is not well constrained by our measurements as we are only using the massive end of the SMF.

#### 5.4. Redshift Evolution

Once we modeled the ICSMFs for different redshift samples, we are able to study the redshift evolution of

TABLE 4  
BEST-FIT SCHECHTER FUNCTION PARAMETERS

$z$ range	$\log \Phi^*$	$\log M_c^*$	$\alpha^*$
$0.1 < z < 0.2$	$16.27 \pm 2.76$	$11.05 \pm 0.05$	$-1.87 \pm 0.34$
$0.2 < z < 0.3$	$6.94 \pm 1.43$	$11.24 \pm 0.04$	$-1.97 \pm 0.21$
$0.3 < z < 0.4$	$3.70 \pm 1.43$	$11.36 \pm 0.07$	$-2.22 \pm 0.29$
$0.4 < z < 0.5$	$2.99 \pm 1.33$	$11.41 \pm 0.08$	$-2.15 \pm 0.27$
$0.5 < z < 0.6$	$2.84 \pm 0.79$	$11.39 \pm 0.06$	$-2.09 \pm 0.22$
$0.6 < z < 0.7$	$3.00 \pm 1.60$	$11.40 \pm 0.11$	$-1.95 \pm 0.35$
$0.7 < z < 0.8$	$1.95 \pm 1.91$	$11.50 \pm 0.17$	$-2.34 \pm 0.51$

The parameters  $\Phi^*$  and  $M_c^*$  are in units of  $10^{-4} \text{Mpc}^{-3} \text{dex}^{-1}$  and  $M_\odot$ , respectively.

the galaxy SHMRs and total SMFs, which are shown in the left and right panels of Figure 11, respectively. It is clear that the slope of the galaxy SHMR is becoming steeper at higher redshifts, while that of the total SMF is correspondingly shallower. The general trend is consistent with the model of Yang et al. (2012) (see their Figure 13), but we have more accurate measurements. We also note that there is only weak evolution in the galaxy SHMR and total SMF from  $z = 0.4$  to  $0.6$ . By fitting a standard Schechter function to the total galaxy SMFs, we find that the characteristic stellar mass only varies from  $10^{11.39} M_\odot$  to  $10^{11.41} M_\odot$  at  $0.4 < z < 0.6$ , which supports the conclusion of Guo et al. (2013) that these massive galaxies are consistent with passive evolution at  $0.4 < z < 0.6$  (see also Tojeiro et al. 2012). Similar conclusions have been reached by Maraston et al. (2013), Montero-Dorta et al. (2016) and Bundy et al. (2017) with the observed galaxy SMFs and luminosity functions. However, a recent study by Bernardi et al. (2016) suggests that for stellar masses obtained using the spectral energy distribution fittings, the different light profile fits would significantly affect the abundance of the massive galaxies. For stellar masses estimated from the PCA analysis of the galaxy spectra, it is less affected by such an effect. But more careful comparisons of the different methods of the stellar mass estimates are necessary to fully resolve all the systematics, which is beyond the scope of the current paper.

## 6. DISCUSSIONS

An important assumption of the completeness function is that for a given stellar mass, the selected galaxies are a random subset of the complete sample. Here we model the central and satellite galaxies separately, but not specifically for the color of galaxies. The targeting strategy of BOSS tends to select more luminous red galaxies than blue ones (see e.g., Figure 1 of Guo et al. 2013). Although galaxies with the same stellar mass but different colors are found to occupy halos of different masses at low redshifts of  $z < 0.2$  (see e.g., More et al. 2011; More et al. 2013; Paranjape et al. 2015; Rodríguez-Puebla et al. 2015; Mandelbaum et al. 2016; Zu & Mandelbaum 2016), the differences in the average halo masses are estimated to be around  $0.1$ – $0.2$  dex at higher redshifts of  $z > 0.2$  (see e.g., the right panel of Figure 7 in Tinker et al. 2013).

In this paper, we are using the whole BOSS galaxy sample to derive the completeness as a function of the stellar mass, which includes the contributions from different populations. Although we estimate the stellar mass incompleteness with the function of Eq. 12, there

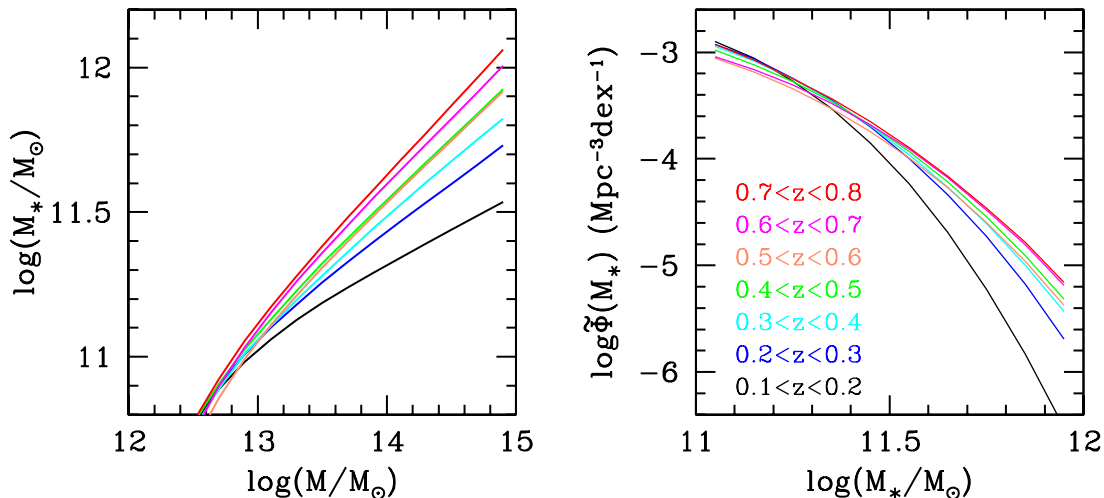


FIG. 11.— Redshift evolution of the galaxy SHMR (left) and total SMF (right). The best-fitting models at different redshifts are shown using lines of different colors.

would be possibly remaining effects of the target selections coming from the mix of the different populations of red and blue galaxies, which potentially have different selection functions. As estimated in [Masters et al. \(2011\)](#) and [Montero-Dorta et al. \(2016\)](#), there are about 25% of blue galaxies in the CMASS sample, while the majority of LOWZ galaxies are LRGs. [Masters et al. \(2011\)](#) proposed to use the color cut of  $g - i > 2.35$  to select the red (elliptical) galaxies in CMASS (see also [Maraston et al. 2013](#)). In order to test whether our derived galaxy total SMF and the SHMR will be affected by the existence of blue galaxies, we impose the color cut of  $g - i > 2.35$  on the typical BOSS sample at  $0.5 < z < 0.6$  to select a roughly homogeneous population of red galaxies. The fraction of blue galaxies removed in this sample is about 21%. Due to the existence of the photometric errors, such a simple color cut does not ensure that we have a purely red galaxy sample, but it still serves as a simple test of the effect of the blue population.

We show in [Figure 12](#) the comparisons between the measurements and models for all galaxies (our fiducial model, shown as black symbols and lines) and those of red galaxies (red symbols and lines). As the red galaxies dominate the SMF at  $M_* > 10^{11} M_\odot$ , the observed clustering measurements of  $w_p(r_p)$  are only slightly affected by the existence of blue galaxies for the lower stellar mass bin, while the derived SHMR and the total galaxy SMF are quite consistent with those obtained from all BOSS galaxies.

The most relevant change for our red galaxy sample is in the stellar mass completeness shown in the top right panel of [Figure 12](#), where the completeness functions of central and satellite galaxies are displayed as the dotted and dashed lines, respectively. Although there seems to be larger decreases of satellite completeness at the massive end, this does not imply that we removed more blue satellite galaxies. Note that at the very massive end, according to comparison between the observed SMFs of all and red galaxies in the bottom right panel, there are almost no blue galaxies at all. Then at the relatively low mass end with  $M_* < 10^{11.3} M_\odot$ , both the central and satellite galaxy completeness functions are slightly reduced by a roughly similar amount (or slightly larger for

the satellite galaxies) due to the removal of blue galaxies. However, considering that the satellite fraction is only about 10% ([White et al. 2011](#); [Guo et al. 2014](#)) at this mass range, the majority of the removed blue galaxies should still be central galaxies. Indeed, the fractional decrease of the observed SMF at the low mass end for the red galaxies is consistent with the decrease of amplitude for the central galaxy completeness.

The above test demonstrates that even though we are using the whole BOSS sample to derive the SHMR and the total galaxy SMF for  $M_* > 10^{11} M_\odot$ , our results are not affected by the existence of blue galaxies. It is caused by the fact that the red galaxies dominate the massive end of the SMF. As discussed in [Tinker et al. \(2013\)](#), the possible differences between the SHMRs of red and blue galaxies are not large enough to significantly change the clustering for these massive galaxies. However, we note that if one goes to much lower mass galaxies where red and blue galaxy populations may have quite different stellar to halo mass relations, one may include a separate component to represent the fractions of red and blue galaxies, respectively. This separation is beyond the scope of current paper and will be explored in a future work.

Considering the construction of the theoretical model, we assumed a double power-law functional form for the central galaxy SHMR and the galaxy selection function is characterized by [Eq. 11](#). A more flexible functional form for the SHMR has been proposed by [Behroozi et al. \(2010\)](#) with a five-parameter model. But as tested in [Behroozi et al. \(2013a\)](#), compared to the four-parameter double power-law model, the additional free parameter mainly helps improve the fits to the SMF at the low mass end at  $M_* < 10^9 M_\odot$ . Adopting the five-parameter SHMR model has minor effects on our results, as we are focusing on the most massive galaxies. From the goodness of our fits to the clustering measurements and observed SMFs in [Figures 6 and 7](#), we conclude that the functional form for the stellar mass completeness is flexible enough for modeling the completeness of the BOSS galaxies, which has already been shown in [Leauthaud et al. \(2016\)](#) and [Montero-Dorta et al. \(2016\)](#) for the completeness as a function of both stellar mass and magnitude, respectively.

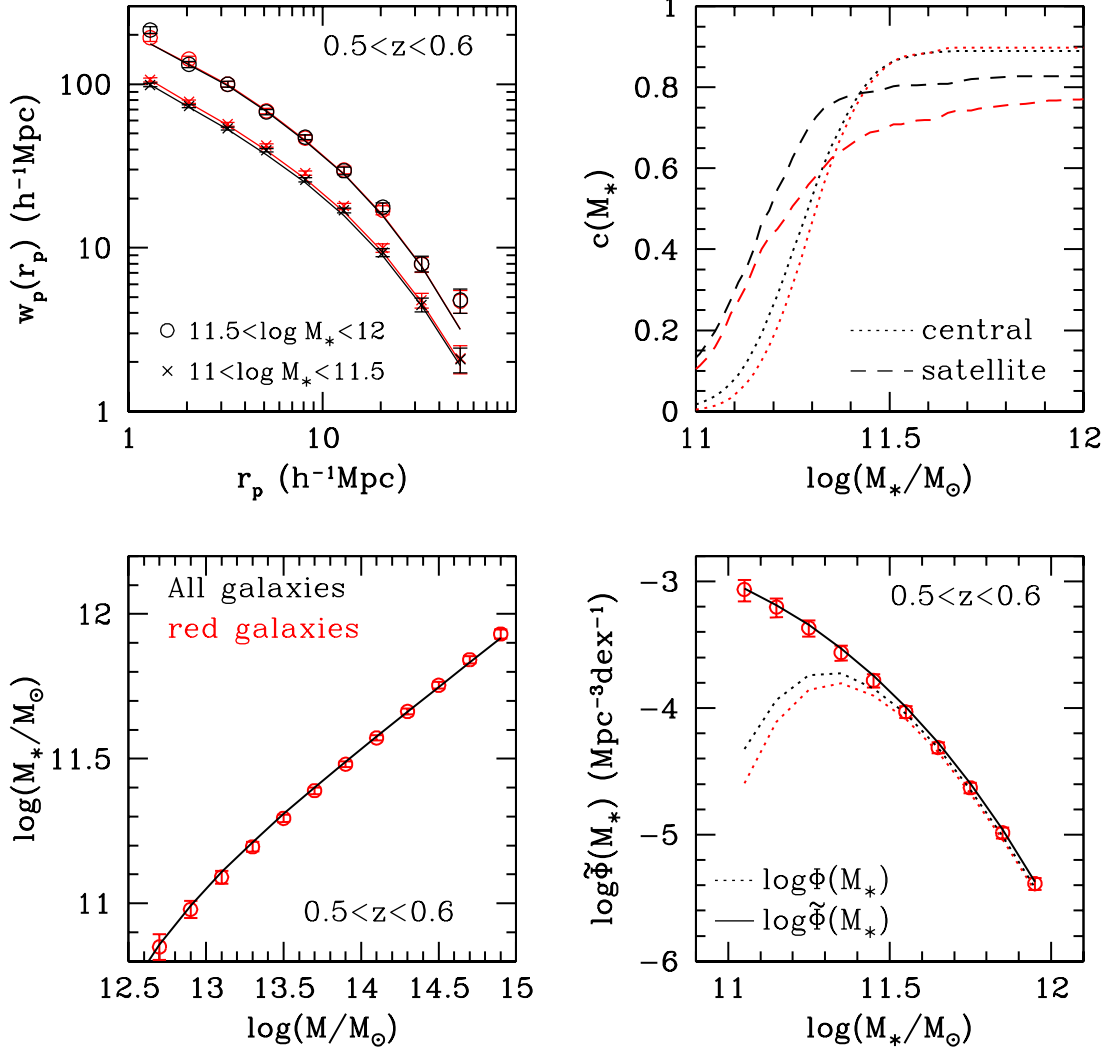


FIG. 12.— Similar to Figure 5, but for the comparisons between the measurements and models for all galaxies (our fiducial model, shown as black symbols and lines) and those of red galaxies (red symbols and lines). We show the completeness functions of central and satellite galaxies in the top right panel as the dotted and dashed lines, respectively. The SHMR of the red galaxies is displayed as the red circles in the bottom left panel, while that of all galaxies is shown as the solid line. The observed SMFs of all and red galaxies are shown as the black and red dotted lines in the bottom right panel, respectively. The predicted total SMF of the red galaxies is shown as the circles and that of all galaxies is represented by the solid line.

Lastly, we assumed the scatter  $\sigma_c$  between the stellar and halo masses, which includes both the contribution from the intrinsic scatter and the statistical errors on the stellar mass estimates, to be a constant value  $\sigma_c = 0.173$ . This value is set according to the stellar mass distribution of central galaxies in groups or halos of given masses (Yang et al. 2009). We have tested that, if we set the amount of the total scatter to be larger or smaller than this value (e.g. with  $\sigma_c = 0.2$  and  $0.15$ , respectively), the SHMRs thus constrained at high mass end will be somewhat lower or larger. However, the SMFs recovered are quite independent of this  $\sigma_c$  value, i.e., roughly consistent within  $1 - \sigma$  errors. In addition, although we do not have strong constraints on the value of  $\sigma_c$ , the inferred  $\chi^2$  of different redshift samples tend to favor our fiducial model of  $\sigma_c = 0.173$  for the BOSS galaxies. Thus we expect that the total galaxy SMFs obtained in this work are robust. We note that the assumed scatter does not include the uncertainties in the systematic effects in the stellar mass estimates caused by the different IMFs, SPS models and

dust attenuation laws, which can be reasonably corrected for using constant offsets (see e.g., Moustakas et al. 2013; Muzzin et al. 2013; Rodríguez-Puebla et al. 2017).

## 7. CONCLUSIONS

In this paper, we have introduced an incomplete conditional stellar mass function (ICSMF) model which is applicable to large-scale galaxy surveys with complicated target selections. By assuming suitable functional forms for the stellar mass completeness function and the galaxy SHMR, we are able to predict the observed galaxy clustering measurements and the incomplete galaxy SMFs, and vice versa, constraining the ICSMF model parameters using these observational measurements. We tested our method using mock galaxy catalogs and then apply it to the BOSS galaxy survey in the redshift range of  $0.1 < z < 0.8$ . We then predicted the galaxy total SMF measurements and central galaxy SHMRs for  $10^{11} M_\odot < M_* < 10^{12} M_\odot$ , which are useful for studying the star formation history and evolution of these massive galaxies.



Our main conclusions are summarized as follows.

- Based on tests using mock galaxy catalogs, we show that the ICSMF model can accurately recover the incompleteness factors, the SHMRs and the galaxy total stellar mass functions. The incompleteness factors thus obtained is independent and more consistent than the methods of involving external measurements from other surveys, which might introduce additional systematics from different surveys.
- By applying our ICSMF model to the BOSS galaxy samples, we find that the BOSS galaxies are more than 80% complete at the massive end for  $0.1 < z < 0.5$ , while for higher redshifts the completeness decreases very fast to around 30% at  $z \sim 0.75$ .
- We obtain accurate measurements of the central galaxy SHMRs for the BOSS galaxies with  $M_* > 10^{11} M_\odot$  from  $z = 0.1$  to  $z = 0.8$ . We find that the high-mass end slope of the SHMR is generally steeper than the previous measurements in literature, varying from about 1/4 to 1/2 in  $0.1 < z < 0.8$ .
- We provide accurate measurements of the total galaxy SMFs for BOSS galaxies within mass range  $10^{11} M_\odot < M_* < 10^{12} M_\odot$  and redshift range

$0.1 < z < 0.8$ , which will provide tighter constraints to the evolution of these massive galaxies.

#### ACKNOWLEDGEMENTS

This work is supported by the National Key Basic Research Program of China (Nos. 2015CB857002, 2015CB857003), national science foundation of China (Nos. 11233005, 11621303, 11655002, 11773049). H.G. acknowledges the support of the 100 Talents Program of the Chinese Academy of Sciences. This work is also supported by a grant from Science and Technology Commission of Shanghai Municipality (Grants No. 16DZ2260200).

We thank the anonymous referee for the helpful comments that significantly improve the presentation of this paper. We thank H. J. Mo and Zheng Zheng for helpful discussions. We gratefully acknowledge the use of the High Performance Computing Resource in the Core Facility for Advanced Research Computing at Shanghai Astronomical Observatory. We acknowledge the Gauss Centre for Supercomputing e.V. ([www.gauss-centre.eu](http://www.gauss-centre.eu)) and the Partnership for Advanced Supercomputing in Europe (PRACE, [www.prace-ri.eu](http://www.prace-ri.eu)) for funding the MultiDark simulation project by providing computing time on the GCS Supercomputer SuperMUC at Leibniz Supercomputing Centre (LRZ, [www.lrz.de](http://www.lrz.de)).

#### REFERENCES

- Abazajian, K. N., Adelman-McCarthy, J. K., Agüeros, M. A., et al. 2009, *ApJS*, 182, 543
- Alam, S., Ata, M., Bailey, S., et al. 2017, *MNRAS*, 470, 2617
- Behroozi, P. S., Conroy, C., & Wechsler, R. H. 2010, *ApJ*, 717, 379
- Behroozi, P. S., Wechsler, R. H., & Conroy, C. 2013a, *ApJ*, 770, 57
- Behroozi, P. S., Wechsler, R. H., & Wu, H.-Y. 2013b, *ApJ*, 762, 109
- Bell, E. F., McIntosh, D. H., Katz, N., & Weinberg, M. D. 2003, *ApJS*, 149, 289
- Berlind, A. A., & Weinberg, D. H. 2002, *ApJ*, 575, 587
- Berlind, A. A., Weinberg, D. H., Benson, A. J., et al. 2003, *ApJ*, 593, 1
- Bernardi, M., Meert, A., Sheth, R. K., et al. 2016, *MNRAS*, 455, 4122
- Bernardi, M., Meert, A., Sheth, R. K., et al. 2013, *MNRAS*, 436, 697
- Bernardi, M., Shankar, F., Hyde, J. B., et al. 2010, *MNRAS*, 404, 2087
- Beutler, F., Blake, C., Colless, M., et al. 2013, *MNRAS*, 429, 3604
- Bruzual, G., & Charlot, S. 2003, *MNRAS*, 344, 1000
- Bundy, K., Leauthaud, A., Saito, S., et al. 2015, *ApJS*, 221, 15
- Bundy, K., Leauthaud, A., Saito, S., et al. 2017, *ApJ*, 851, 34
- Cacciato, M., van den Bosch, F. C., More, S., Mo, H., & Yang, X. 2013, *MNRAS*, 430, 767
- Chabrier, G. 2003, *PASP*, 115, 763
- Charlot, S., & Fall, S. M. 2000, *ApJ*, 539, 718
- Chen, Y.-M., Kauffmann, G., Tremonti, C. A., et al. 2012, *MNRAS*, 421, 314
- Coil, A. L., Blanton, M. R., Burles, S. M., et al. 2011, *ApJ*, 741, 8
- Colless, M. 1999, *Philosophical Transactions of the Royal Society of London Series A*, 357, 105
- Coupon, J., Kilbinger, M., McCracken, H. J., et al. 2012, *A&A*, 542, A5
- Davidzon, I., Bolzonella, M., Coupon, J., et al. 2013, *A&A*, 558, A23
- Davidzon, I., Ilbert, O., Laigle, C., et al. 2017, *A&A*, 605, A70
- Davis, M., & Peebles, P. J. E. 1983, *ApJ*, 267, 465
- Dawson, K. S., Schlegel, D. J., Ahn, C. P., et al. 2013, *AJ*, 145, 10
- Dawson, K. S., Kneib, J.-P., Percival, W. J., et al. 2016, *AJ*, 151, 44
- DESI Collaboration, Aghamousa, A., Aguilar, J., & et al. 2016, [arXiv:1611.00036](https://arxiv.org/abs/1611.00036)
- Eisenstein, D. J., Weinberg, D. H., Agol, E., & et al. 2011, *AJ*, 142, 72
- Eisenstein, D. J., Annis, J., Gunn, J. E., et al. 2001, *AJ*, 122, 2267
- Fioc, M., & Rocca-Volmerange, B. 1997, *A&A*, 326, 950
- Guo, H., Zehavi, I., Zheng, Z., et al. 2013, *ApJ*, 767, 122
- Guo, H., Zheng, Z., Zehavi, I., et al. 2014, *MNRAS*, 441, 2398
- Guo, H., Zheng, Z., Zehavi, I., et al. 2015, *MNRAS*, 453, 4368
- Guo, H., Zheng, Z., Behroozi, P. S., et al. 2016, *MNRAS*, 459, 3040
- Guo, Q., White, S., Li, C., & Boylan-Kolchin, M. 2010, *MNRAS*, 404, 1111
- Ilbert, O., McCracken, H. J., Le Fèvre, O., et al. 2013, *A&A*, 556, A55
- Jing, Y. P., Mo, H. J., & Börner, G. 1998, *ApJ*, 494, 1
- Kauffmann, G., Heckman, T. M., White, S. D. M., et al. 2003, *MNRAS*, 341, 33
- Klypin, A., Yepes, G., Gottlöber, S., Prada, F., & Heß, S. 2016, *MNRAS*, 457, 4340
- Kroupa, P. 2001, *MNRAS*, 322, 231
- Landy, S. D., & Szalay, A. S. 1993, *ApJ*, 412, 64
- Leauthaud, A., Tinker, J., Bundy, K., et al. 2012, *ApJ*, 744, 159
- Leauthaud, A., Bundy, K., Saito, S., et al. 2016, *MNRAS*, 457, 4021
- Li, C., & White, S. D. M. 2009, *MNRAS*, 398, 2177
- Lin, Y.-T., Mandelbaum, R., Huang, Y.-H., et al. 2016, *ApJ*, 819, 119
- Mandelbaum, R., Seljak, U., Cool, R. J., et al. 2006, *MNRAS*, 372, 758
- Mandelbaum, R., Wang, W., Zu, Y., et al. 2016, *MNRAS*, 457, 3200
- Maraston, C., & Strömbäck, G. 2011, *MNRAS*, 418, 2785
- Maraston, C., Pforr, J., Henriques, B. M., et al. 2013, *MNRAS*, 435, 2764
- Martin, D. C., Fanson, J., Schiminovich, D., et al. 2005, *ApJ*, 619, L1
- Masters, K. L., Maraston, C., Nichol, R. C., et al. 2011, *MNRAS*, 418, 1055

- McCracken, H. J., Wolk, M., Colombi, S., et al. 2015, *MNRAS*, 449, 901
- Mitchell, P. D., Lacey, C. G., Baugh, C. M., & Cole, S. 2013, *MNRAS*, 435, 87
- Miyatake, H., More, S., Mandelbaum, R., et al. 2015, *ApJ*, 806, 1
- Mo, H. J., Jing, Y. P., & White, S. D. M. 1996, *MNRAS*, 282, 1096
- Montero-Dorta, A. D., Bolton, A. S., Brownstein, J. R., et al. 2016, *MNRAS*, 461, 1131
- More, S., van den Bosch, F. C., Cacciato, M., et al. 2011, *MNRAS*, 410, 210
- More, S. 2012, *ApJ*, 761, 127
- More, S., van den Bosch, F. C., Cacciato, M., et al. 2013, *MNRAS*, 430, 747
- Moster, B. P., Naab, T., & White, S. D. M. 2013, *MNRAS*, 428, 3121
- Moster, B. P., Somerville, R. S., Maulbetsch, C., et al. 2010, *ApJ*, 710, 903
- Moustakas, J., Coil, A. L., Aird, J., et al. 2013, *ApJ*, 767, 50
- Muzzin, A., Marchesini, D., Stefanon, M., et al. 2013, *ApJ*, 777, 18
- Norberg, P., Baugh, C. M., Hawkins, E., et al. 2001, *MNRAS*, 328, 64
- Paranjape, A., Kovač, K., Hartley, W. G., & Pahwa, I. 2015, *MNRAS*, 454, 3030
- Parejko, J. K., Sunayama, T., Padmanabhan, N., et al. 2013, *MNRAS*, 429, 98
- Peacock, J. A., & Smith, R. E. 2000, *MNRAS*, 318, 1144
- Pérez-González, P. G., Rieke, G. H., Villar, V., et al. 2008, *ApJ*, 675, 234
- Planck Collaboration. 2014, *A&A*, 571, A16
- Prakash, A., Licquia, T. C., Newman, J. A., et al. 2016, *ApJS*, 224, 34
- Raichoor, A., Comparat, J., Delubac, T., et al. 2017, *MNRAS*, 471, 3955
- Reddick, R. M., Wechsler, R. H., Tinker, J. L., & Behroozi, P. S. 2013, *ApJ*, 771, 30
- Reid, B., Ho, S., Padmanabhan, N., et al. 2016, *MNRAS*, 455, 1553
- Rodríguez-Puebla, A., Avila-Reese, V., Yang, X., et al. 2015, *ApJ*, 799, 130
- Rodríguez-Puebla, A., Drory, N., & Avila-Reese, V. 2012, *ApJ*, 756, 2
- Rodríguez-Puebla, A., Primack, J. R., Avila-Reese, V., & Faber, S. M. 2017, *MNRAS*, 470, 651
- Rodríguez-Torres, S. A., Chuang, C.-H., Prada, F., et al. 2016, *MNRAS*, 460, 1173
- Saito, S., Leauthaud, A., Hearin, A. P., et al. 2016, *MNRAS*, 460, 1457
- Salpeter, E. E. 1955, *ApJ*, 121, 161
- Santini, P., Ferguson, H. C., Fontana, A., et al. 2015, *ApJ*, 801, 97
- Schechter, P. 1976, *ApJ*, 203, 297
- Scoccimarro, R., Sheth, R. K., Hui, L., & Jain, B. 2001, *ApJ*, 546, 20
- Seljak, U. 2000, *MNRAS*, 318, 203
- Shankar, F., Guo, H., Bouillot, V., et al. 2014, *ApJ*, 797, L27
- Takada, M., Ellis, R. S., Chiba, M., et al. 2014, *PASJ*, 66, R1
- Tinker, J. L., Leauthaud, A., Bundy, K., et al. 2013, *ApJ*, 778, 93
- Tinker, J. L., Weinberg, D. H., Zheng, Z., & Zehavi, I. 2005, *ApJ*, 631, 41
- Tinker, J. L., Brownstein, J. R., Guo, H., et al. 2017, *ApJ*, 839, 121
- Tomczak, A. R., Quadri, R. F., Tran, K.-V. H., et al. 2014, *ApJ*, 783, 85
- Tojeiro, R., Percival, W. J., Wake, D. A., et al. 2012, *MNRAS*, 424, 136
- van den Bosch, F. C., Aquino, D., Yang, X., et al. 2008, *MNRAS*, 387, 79
- van den Bosch, F. C., More, S., Cacciato, M., Mo, H., & Yang, X. 2013, *MNRAS*, 430, 725
- Wang, L., & Jing, Y. P. 2010, *MNRAS*, 402, 1796
- Wang, H., Mo, H. J., Chen, S., et al. 2018, *ApJ*, 852, 31
- Wang, Y., Yang, X., Mo, H. J., & van den Bosch, F. C. 2007, *ApJ*, 664, 608
- White, M., Blanton, M., Bolton, A., et al. 2011, *ApJ*, 728, 126
- Yang, X., Mo, H. J., Jing, Y. P., van den Bosch, F. C., & Chu, Y. 2004, *MNRAS*, 350, 1153
- Yang, X., Mo, H. J., & van den Bosch, F. C. 2003, *MNRAS*, 339, 1057
- Yang, X., Mo, H. J., van den Bosch, F. C., et al. 2007, *ApJ*, 671, 153
- Yang, X., Mo, H. J., & van den Bosch, F. C. 2009, *ApJ*, 695, 900
- Yang, X., Mo, H. J., van den Bosch, F. C., et al. 2013, *ApJ*, 770, 115
- Yang, X., Mo, H. J., van den Bosch, F. C., Zhang, Y., & Han, J. 2012, *ApJ*, 752, 41
- Yang, X., Zhang, Y., Lu, T., et al. 2017, *ApJ*, 848, 60
- Yang, X., Zhang, Y., Wang, H., et al. 2017, *arXiv:1712.00883*
- York, D. G., Adelman, J., Anderson, Jr., J. E., et al. 2000, *AJ*, 120, 1579
- Zehavi, I., Blanton, M. R., Frieman, J. A., et al. 2002, *ApJ*, 571, 172
- Zehavi, I., Eisenstein, D. J., Nichol, R. C., et al. 2005, *ApJ*, 621, 22
- Zehavi, I., Zheng, Z., Weinberg, D. H., et al. 2011, *ApJ*, 736, 59
- Zheng, Z., Berlind, A. A., Weinberg, D. H., et al. 2005, *ApJ*, 633, 791
- Zheng, Z., Coil, A. L., & Zehavi, I. 2007, *ApJ*, 667, 760
- Zheng, Z., Zehavi, I., Eisenstein, D. J., Weinberg, D. H., & Jing, Y. P. 2009, *ApJ*, 707, 554
- Zheng, Z., & Guo, H. 2016, *MNRAS*, 458, 4015
- Zu, Y., & Mandelbaum, R. 2015, *MNRAS*, 454, 1161
- Zu, Y., & Mandelbaum, R. 2016, *MNRAS*, 457, 4360